

UNCERTAINTY ANALYSIS OF STEADY-STATE CALORIMETRIC EMISSIVITY MEASUREMENTS

A Dissertation
presented to
the Faculty of the Graduate School

at the University of Missouri

In Partial Fulfillment
of the Requirements for the Degree
Doctor of Philosophy

by
KYLE L. WALTON

Dr. Robert V. Tompson, Jr.

Dissertation Supervisor

Dr. Sudarshan K. Loyalka

Dissertation Co-Supervisor

Dr. Tushar K. Ghosh

Dissertation Co-Supervisor

DECEMBER 2017

© Copyright by Kyle Lucas Walton 2017

All Rights Reserved

The undersigned, appointed by the Dean of the Graduate School, have examined the dissertation entitled

**UNCERTAINTY ANALYSIS OF STEADY-STATE
CALORIMETRIC EMISSIVITY MEASUREMENTS**

presented by Kyle L. Walton,

candidate for the degree of Doctor of Philosophy,

and hereby certify that, in their opinion, it is worthy of acceptance.

Dr. Robert V. Tompson, Jr.

Dr. Sudarshan K. Loyalka

Dr. Tushar K. Ghosh

Dr. Mark A. Prelas

Dr. Dabir S. Viswanath

In loving memory of Susan Walton.

ACKNOWLEDGMENTS

I am grateful to the faculty of the Nuclear Science and Engineering Institute (NSEI) for giving me the opportunity to learn and work under them. I am particularly thankful to my advisor, Dr. Robert Tompson, and co-advisors, Drs. Sudarshan Loyalka and Tushar Ghosh. Their combination of skill sets and problem solving approaches was truly unique. I thank them for not giving up on me when other projects did not go as expected. I thank my committee members, Drs. Mark Prelas and Dabir Viswanath, for providing me with guidance in experimental work and preparation of papers.

I also acknowledge several staff members at the University of Missouri. NSEI staff members, James Bennett and Latricia Vaughn, were important in completion of my degree. They have gone above and beyond countless times to support faculty and students of the NSEI. The machinists and technicians at the MU Physics Shop and Engineering Technical Services were vital in making specialized components for the various experimental projects I was involved with. I have been very fortunate to learn from their expertise. It has also made me a better researcher. Finally, I thank the MU Library staff for helping me obtain even the most obscure works.

I have come across too many students to thank individually. Those who were my mentors or role models when I joined the NSEI will always be remembered. Several have become close friends and have helped get me through these final years—you know who are!

I am also thankful for the U.S Department of Energy Nuclear Energy University Programs (NEUP) for funding this work and the Nuclear Regulatory Commission for

supporting me with their fellowship. The NEUP also funded me and my work on my previous project

Finally, I give thanks to my family for their endless support and understanding.

TABLE OF CONTENTS

ACKNOWLEDGMENTS	ii
LIST OF FIGURES	vi
LIST OF TABLES	viii
ABSTRACT	x
CHAPTER	
1. INTRODUCTION.....	1
1.1. Emissivity.....	1
1.2. Emissivity Measurements	1
1.3. Scope and Organization	2
2. BACKGROUND	4
2.1. Overview	4
2.2. Emissivity.....	4
2.3. Uncertainty Propagation	8
3. EXPERIMENTAL METHOD.....	16
3.1. Overview	16
3.2. Sample Preparation	16
3.3. Construction of Vacuum Calorimeter	19
3.4. Estimation of Non-Radiative Heat Losses and Non-Grayness	25
3.5. Experimental Procedure.....	34

4. UNCERTAINTY ANALYSIS.....	36
4.1. Overview	36
4.2. Measurement Model	36
4.3. Sources of Error	43
4.4. Calculation of Uncertainties.....	53
5. RESULTS	59
5.1. Overview	59
5.2. Instrumentation Uncertainty	59
5.3. Emissivity Calculation Uncertainty Budget.....	63
5.4. Uncertainty in Data Sets	68
6. CONCLUSIONS	74
APPENDIX	
MATERIAL DATA	76
A.1. Thermal Conductivity	76
A.2. Emissivity.....	78
BIBLIOGRAPHY.....	80
VITA.....	86

LIST OF FIGURES

Figure	Page
2.1 An illustration of measurement accuracy and precision. Precision is the spread in the light blue dots, while accuracy indicates how close the central tendency is close to the center of the target.....	9
3.1 (a) TC placement from the distance from one end and gap between TC leads. (b) Thermoelement layout for specimen TCs where Ch is chromel and Al is alumel. Voltage taps are on each alumel thermoelement (connected at temperature DAQ). Voltage drops are determined at each adjacent alumel lead and at additional pairs indicated above.....	18
3.2 Side view of the emissometer emphasizing the specimen holder and vacuum system. The numbered labels are: (1) dead weight to prevent buckling from thermal expansion, (2) ceramic coupler to insulate specimen from dead weight, (3) low-impedance electrical cable, (4) specimen, (5) Macor [®] posts for connected spot-welded TCs to heavier gauge TC wire for feedthroughs, and (6) upper holder electrode that is adjustable for different length specimens.	20
3.3 Top view of emissometer showing the layout in the base well. The labeled components are: (a) K-type TC feedthroughs, (b) hall-effect sensor, (c) DC power supply, and (d) polarity-reversing switch.	21
3.4 Statechart of the LabVIEW [®] VI for reading and recording data for calorimetric emissometers by the NSEI group. Dashed lines indicate events returning the program to a pervious state.....	24

3.5	Heat loss and gain mechanisms for a test section including ohmic heating, thermal conduction in the specimen to the ends, thermal conduction in the TC leads, emitted radiation, and absorbed radiation (from chamber walls no reflection).	27
4.1	Conceptual diagram of the measurement model. Dashed boxes indicate measurement systems and their measured quantities. The indices i, j , and k indicate the number of voltage drops (total: 4), specimen temperatures (total: 5), and wall temperatures (total: 2).	38
4.2	Diagrams for electrical DC current measurement sub-systems for the calorimetric emissometer built by the NSEI group: (a) shunt resistor and amplifier setup and (b) present setup consisting of HES transducer directly read by the NI-USB-6251.....	40
5.1	Standard uncertainties in the form of errors bars for 0.254 mm thick Hastelloy X (top graph) and 0.409 mm thick Inconel 718 (bottom graph). Blue points are data with emissivity with relative uncertainty greater than 5%. Both surfaces are ‘as-received’	70
5.2	Standard uncertainties in the form of errors bars for Alloy 718 for a low-emittance (top graph) and high-emittance surface conditions (bottom graph). Blue points are data with emissivity with a relative uncertainty greater than 5%.....	71
5.3	Standard uncertainties in emissivity for oxidized SS 316S in the form of errors bars	73

LIST OF TABLES

Table	Page
3.1 Calculation of systematic effects on Hastelloy X for emissivity determined between TC #2 and TC #4.....	33
4.1 Polynomial coefficients for inverse function for K-type thermocouples.	43
4.2 Errors sources for dimensional measurement devices.....	45
4.3 Values for resolution and gain and offset errors for the NI-USB-625.	46
4.4 Cross-test test on a Hastelloy X strip at -30 A for NI-USB-6251.....	47
4.5 Errors sources for the NI-USB-6251.....	48
4.6 Errors sources for K-type TCs and temperature DAQ.	50
4.7 A list of error sources for the DC power supply unit and HES transducer.	52
4.8 A list of sensitivity coefficients for the combined uncertainty by Eq. 4.27.	58
5.1 Absolute accuracy and resolution of NI-USB-6251 for typical values of the voltage drops over 1.27 cm to 2.54 cm long sections.	60
5.2 Uncertainty components for DC current measurements in A.....	61
5.3 Standard uncertainty of TC measurements neglecting repeatability error. DAQ accuracy and resolution are constant for all temperatures.....	62
5.4 Uncertainty budget for the emissivity calculation for Alloy 718 between TC #2 and TC #4 at the lowest temperature.....	64
5.5 Uncertainty budget for the emissivity calculation for Alloy 718 between TC #2 and TC #4 at the highest temperature.....	64
5.6 Emissivity and standard of Alloy 718 ‘as-received’ Run #2 from higher order Taylor Series.	65

5.7	Uncertainty budget for the emissivity calculation for Alloy 718 between TC #1 and TC #5 at the lowest temperature.....	66
5.8	Uncertainty budget for the emissivity calculation for Alloy 718 between TC #1 and TC #5 at the highest temperature.....	66
5.9	Uncertainty budget for the heat generated between TC #2 to TC #4 using the voltage drop measured between TC #2 and TC #4.	67
5.10	Uncertainty budget for the heat generated between TC #2 to TC #4 by adding the voltage drops between TC #2 to TC #3 and TC #3 to TC #4.	68
5.11	Uncertainty budget for the heat generated between TC #1 to TC #5 by adding the voltage drops measured between adjacent TC pair.	68
A.1	Thermal conductivity of Hastelloy X.	76
A.2	Thermal conductivity of alumel.	77
A.3	Thermal conductivity of chormel.	77
A.4	Total hemispherical emissivity of alumel.....	78
A.5	Total hemispherical emissivity of chormel.	79

ABSTRACT

Determining the accuracy and uncertainty in total hemispherical emissivity data is important in the uncertainty quantification of predictive models using radiant heat transfer. Very High Temperatures Reactors (VHTR) are intended to passively remove decay from fission products by the emissive power of the structural materials and ultimately the reactor pressure vessel into the surroundings. By removing this decay heat, the reactor and its fuel will remain intact. Total hemispherical emissivity data must be obtained for specific materials with specific surface conditions. The goal of this dissertation is to determine the uncertainty on previously experimental data on the emissivity of VHTR materials using a calorimetric emissometer constructed according to ASTM C835-06. An additional purpose is to provide a model for which the uncertainty in other ASTM C835-06 designs, or similar calorimetric emissometers, can be evaluated. This is achieved by using an uncertainty analysis described by the JCGM 100:2008: Evaluation of measurement data — Guide to the expression to the uncertainty in measurement, or GUM. A thorough examination of the calorimeter design and experimental procedure is given to identify and characterize errors in the measurement of raw data and calculation of total hemispherical emissivity. Uncertainty is reported for select cases to demonstrate the minimum and maximum values.

CHAPTER 1

INTRODUCTION

1.1 Emissivity

Radiant heat transfer is important when an object has a high absolute temperature and is separated from other objects and surfaces with a transparent medium or vacuum. It is one of the three modes of heat transfer including convection and conduction. Emissivity is a dimensionless quantity that is the ratio of the emissive power of a real surface to the emissive power of a black body, which is a perfect emitter and absorber of electromagnetic (EM) radiation. As with many other measurement processes, the measurement of emissivity is prone to errors and uncertainties. There is a need to constantly improve the quality of experimental measurements. Yet, determining emissivity data and its uncertainty is important for non-contact thermography^{1, 2} and uncertainty quantification for models utilizing radiant heat transfer like atmospheric re-entry of spacecraft³ and progression of nuclear accidents^{4, 5}.

1.2 Emissivity Measurements

Measurements of emissivity can be divided into two general classes: (i) measuring emitted, or reflected, EM radiation from the specimen surface (radiometric) or (ii) measuring the radiant heat transfer from the specimen to its surroundings (calorimetric). The thermal radiative properties such as emissivity depend on the wavelength and direction of EM radiation and the temperature of the body. For this reason, radiometric and calorimetric techniques should be viewed as complementary to one another. Radiometric techniques can measure emissivity at specific wavelengths and directions. However,

spectrometers capable of measuring a wide range of wavelengths and/or directions can be complex. Emissometers based on calorimetry measure the emissive power of the body over all wavelengths (total) and directions (hemispherical). Though radiometric and calorimetric experiments can vary in design and principal of operation, some select designs have gained wide spread use among researchers and have even been standardized. A type of “hot filament” steady-state calorimetric emissometer has been standardized under the ASTM C835-06 for total hemispherical emissivity.⁶

The ASTM C835-06 and supporting literature provides a good treatment of systematic error, but the determination of uncertainty in total hemispherical emissivity is not as developed. This standard reports a basic uncertainty propagation of uncertainties obtained from interlaboratory testing with two labs. The uncertainties using a material for low-emissivity (bright-finished aluminum) and high-emissivity (painted SS 304) had uncertainties around 5%. Compton⁷ reported relative uncertainties of select points for several different alloys for their ASTM C835-06 calorimeter. The emissivity had relative uncertainties of 3.2% to 4.7%, consistent with the standard. Recent work by Fu et al.⁸ reported relative uncertainties of 1.1 % for all data points. However insufficient details are given to allow guidance to assess other ASTM C835-06 designs or how to attain their stated uncertainties. Uncertainty analyses in accordance to the GUM are recently available for radiometric emissometers.^{9; 10}

1.3 Scope and Organization

The goal of this dissertation is to develop an uncertainty analysis that can be applied to hot-filament style calorimetric emissometers, particularly the type described by ASTM C835-06. The uncertainty analysis will allow to determine the combined uncertainty of

previous works published by the author's host group at the University of Missouri (referred to as NSEI hereafter) and also will be general enough to evaluate other systems or assist in the design of new systems. The use of DC current for ohmic heating and digital acquisition in the calorimetric emissometers used by NSEI should represent one of the more complicated designs to evaluate. AC currents eliminate certain artifacts, but also present their own challenges. It is hoped that the uncertainty analysis will be able to incorporate any new sources of error that will arise in verification by interlaboratory testing per ASTM E691-16.

The nature of this work and the results are discussed in the five remaining chapters of this dissertation. Chapter 2 provides basic definitions and theory for emissivity and an overview of the GUM methodology and its calculation of uncertainty. Chapter 3 describes the experimental system and process that the uncertainty analysis will be applied to. The development of the measurement model, examination of errors sources, and the computation of the combined are given in Chapter 4. Results of the uncertainty analysis will be in Chapter 5. Chapter 6 concludes the dissertation with the findings of this uncertainty analysis and provides a brief commentary on its use and further development.

CHAPTER 2

BACKGROUND

2.1 Overview

An introduction to emissivity and uncertainty propagation is given here. It is important to clarify several concepts to properly interpret the methods in this study. Radiative properties of materials are briefly defined followed by a discussion of total hemispherical emissivity calculations in calorimetric measurements and black body theory. There are two main approaches to uncertainty analysis. A thorough discussion is provided to help eliminate common misconceptions of the GUM analysis and to justify its use in this study. Equations for combining uncertainties will be provided here as well.

2.2 Emissivity

Many theories and models exist for describing the interaction of EM radiation with matter. The phenomenological properties of absorptivity, reflectivity, and transmissivity are convenient for most applications. They are dimensionless quantities that describe the fraction of energy, or intensity, of EM radiation interacting with a material. From the conservation of energy, the absorptivity (α), reflectivity (ρ), and transmissivity (τ) of a material add to:

$$\alpha + \rho + \tau = 1 . \quad (2.1)$$

Equation 2.1 can be generalized to add emissivity, but emissivity and absorptivity are equal for thermal radiation. Equation 2.1 is useful for radiometric measurements of emissivity where emissivity can be measured directly or indirectly from reflectivity of a surface.

These quantities are functions of the wavelength and direction of EM radiation and temperature of material. Thus, data is described in terms of their spectral or angular distributions. The optical properties depend also on surface condition like roughness and oxidation. When a quantity is measured for specific surface conditions, the suffix -ance is used for the optical properties, i.e. absorptivity vs absorptance.

Calorimetric techniques measure the total hemispherical emittance of materials. In calorimetric measurements, the heat loss of a radiating body in an enclosure is measured by the temperature difference between the body and its enclosure. The net heat transfer for two concentric surfaces is given by:

$$Q_1 = \frac{\sigma A_1 (T_1^4 - T_2^4)}{\frac{1}{\varepsilon_1} + \frac{A_1}{A_2} \left(\frac{1}{\varepsilon_2} - 1 \right)} \quad (2.2)$$

where Q_1 is the net radiant heat transfer from the test section in W, A_1 the surface area of test section in m^2 , ε_1 is the emissivity of test section, T_1 is the average temperature of test section in K, A_2 the surface area of the chamber walls in m^2 , ε_2 is the emissivity of the chamber walls, and T_2 is the average temperature of the chamber walls in K.¹¹ The term in the denominator is the shape, or view, factor for the specified geometry. ASTM C835-06 requires that $\varepsilon_2 \geq 0.8$ and $A_1/A_2 < 0.01$ such that:

$$\frac{1}{\varepsilon_1} \gg \frac{A_1}{A_2} \left(\frac{1}{\varepsilon_2} - 1 \right). \quad (2.3)$$

When Eq. 2.3 is satisfied, Eq. 2.2 reduces to the Stefan-Boltzmann equation for the radiating body:

$$\varepsilon_1 = \frac{Q_1}{\sigma A_1 (T_1^4 - T_2^4)} \quad (2.4)$$

where σ is the Stefan-Boltzmann constant in $W m^{-2} K^{-4}$.⁶ In contrast, most radiometric

setups tend to measure a narrow band of wavelengths normal to the surface. In principle, spectral angular data can be integrated to obtain total hemispherical quantities. Touloukian et al.¹² provides a good summary and overview of some common radiometric and calorimetric techniques used at the time.

Blackbody theory is vital to the definition of emissivity of real materials and relationship of emissivity and absorptivity. A blackbody is an idealized object that completely absorbs EM radiation striking on its surface. Thus, it is a perfect emitter of radiation as it was then understood a good absorber was a good emitter. The concept of a blackbody was formalized by Gustav Kirchhoff in 1860 when he first postulated his law of thermal radiation.¹³ In the simplest case, Kirchhoff's law equates an object's emissivity to its absorptivity when a radiating object is in thermal equilibrium with an enclosure. Both the body and the enclosure are at the same temperature. A more general statement of Kirchhoff's law of thermal radiation is the ratio of the spectral emissive power of a real surface to its absorptivity is equal to the spectral emissive power of a black body, or:

$$\frac{e(\lambda, T)}{\alpha(\lambda, T)} = e_{\text{BB}}(\lambda, T) \quad (2.5)$$

where λ is the wavelength of EM radiation in μm , T is the temperature in K, $e(\lambda, T)$ is the spectral emissive power of a real surface in W per unit area (m^2) per unit wavelength (μm^1), $\alpha(\lambda, T)$ is the absorptivity of the real surface (unitless), and $e_{\text{BB}}(\lambda, T)$ is the spectral emissive power of a black body in W per unit area (m^2) per unit wavelength (μm^1).¹⁴ In 1860, Kirchhoff had a less refined version of Eq. 2.5 where $e_{\text{BB}}(\lambda, T)$ was called a universal function of λ and T .¹³ Though he knew the importance of $e_{\text{BB}}(\lambda, T)$, Kirchhoff was only able to deduce a few properties of this function from experimental observations.

In the following decades, much experimental and theoretical work was done to develop an understanding of $e_{\text{BB}}(\lambda, T)$.

Max Planck was the first to determine a mathematical expression of $e_{\text{BB}}(\lambda, T)$ for all wavelengths in the EM spectrum. The assumptions Planck needed to derive his equation started a paradigm shift that led to quantum mechanics. Wilhelm Wien proposed a semi-empirical expression for $e_{\text{BB}}(\lambda, T)$ that was only valid at short wavelengths. Motivated by Wien's work Planck developed his law for spectral emissive power:

$$e_{\text{BB}}(\lambda, T) = \frac{2\pi hc^2}{\lambda^5 \left[\exp\left(\frac{hc}{\lambda k_{\text{B}} T} - 1\right) \right]} \quad (2.6)$$

where h is Planck's constant in J s, c is the speed of light in m s^{-1} , k_{B} is the Boltzmann's constant in J K^{-1} , and λ is the wavelength in μm .¹¹ Around the time Planck developed his equation, Lord Rayleigh and Sir James Jeans developed an expression using classical physics that was only good for long wavelengths. The beauty of Planck's law is that Wien's and Rayleigh-Jean's laws are asymptotic cases of Planck's law for short and long wavelengths respectively. Planck's law is a necessity in radiometric experiments, because one measures the radiance of a surface rather than emissivity. Emissivity is determined by measuring the radiance black body cavity reference under the same optical setup as the specimen.

For calorimetric measurements, Kirchhoff's and Planck's laws are useful in understanding the equilibrium of a specimen with the surrounding radiation field from the enclosure. A consequence of Planck's law, a body or surface will emit EM radiation of any temperature above absolute zero. This EM radiation tends to have a longer wavelength at lower temperatures and a shorter wavelength at higher temperatures. Though the blackened

interior of the calorimeter may be approximated as a black body emitter, the absorptivity of the specimen to this radiation is unknown. Thus, there is an error to assuming that the specimen's absorptivity of the surrounding EM radiation is equal to the emissivity of the radiation it is emitting. If the specimen was a gray-body, the emissivity and absorptivity would be independent of wavelength and would be equal.¹¹ This type of systematic effect in calorimetric and radiometric measurements is called the non-gray error. When the specimen and enclosure have the same temperature, Kirchhoff's law would be satisfied, but no heat would be transferred to perform a calorimetric measurement.

2.3 Uncertainty Propagation

The quality of measurement processes and devices is typically described in terms of accuracy and precision. Accuracy is how close the measured value is to the 'true' value of the quantity of interest whereas precision describes the consistency of the measured value. Figure 2.1 illustrates how measurements can vary in both precision and accuracy and that these terms cannot be interchanged. A measurement can have a high accuracy, but could be very imprecise. Most approaches sort errors into systematic and random errors as they affect a measurement's accuracy and precision respectively. Yet, the traditional view of the non-statistical behavior of systematic errors has created controversy particularly in combining systematic and random uncertainties for total combined uncertainty. The GUM method avoids this issue by combining the standard deviations rather than confidence intervals or a similar expanded uncertainty, but assumes all errors are random variables.

Usually, the quantity of interest in a measurement is calculated by one or more measured input quantities. Uncertainty propagation aims to determine the uncertainty in calculated quantity when the variables themselves have uncertainties. While there are

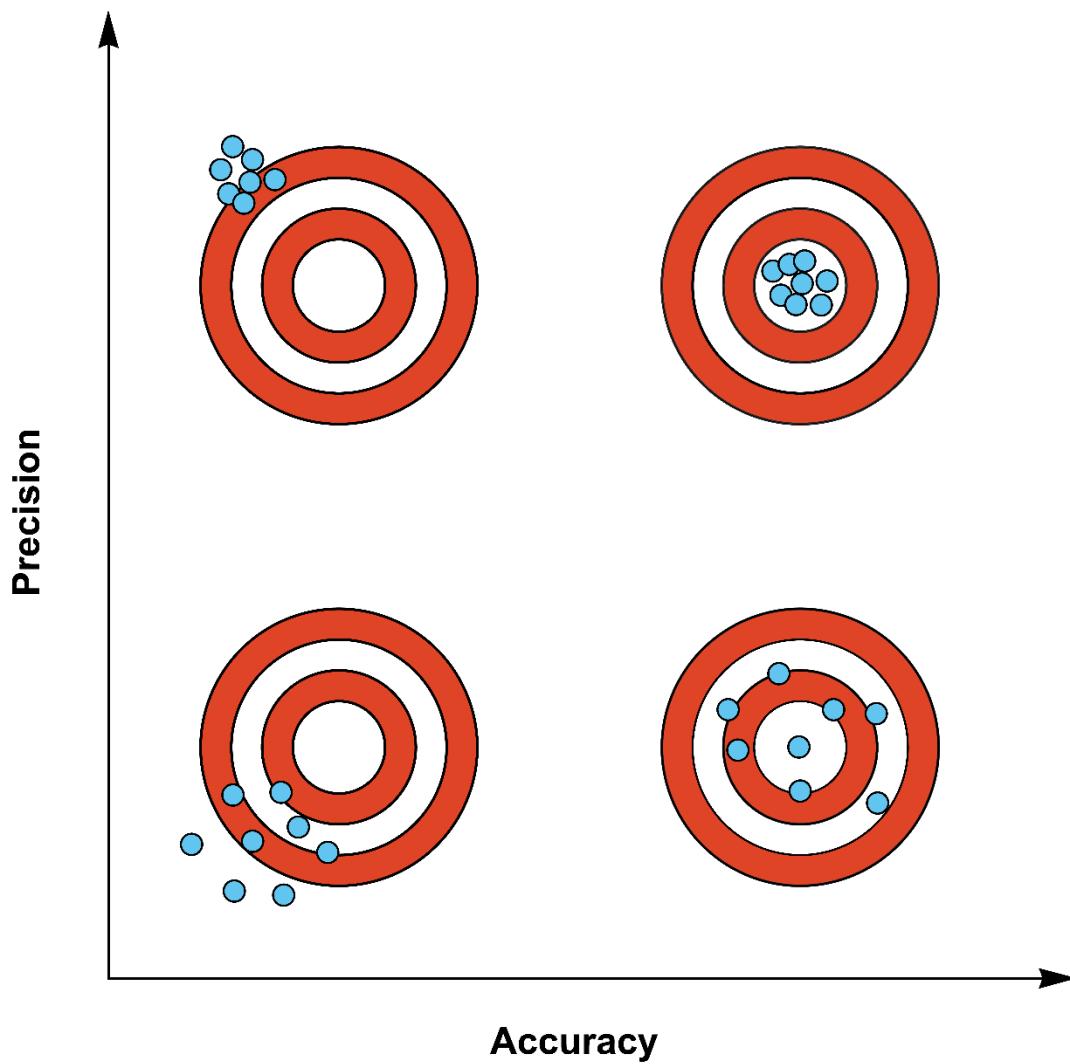


Figure 2.1: An illustration of measurement accuracy and precision. Precision is the spread in the light blue dots, while accuracy indicates how close the central tendency is close to the center of the target.

several methods available, uncertainty propagation of a function $f(x)$ using the expectation value and variance of its Taylor's expansion is the most common method for propagating uncertainties. Ignoring higher order terms, the quantity y calculated from correlated input quantities (x_1, x_2, \dots, x_N) by the function:

$$y = f(x_1, x_2, \dots, x_N) \quad (2.7)$$

has a combined uncertainty¹⁵:

$$u_c^2(y) = \sum_{i=1}^N c_i^2 u^2(x_i) + 2 \sum_{i=1}^{N-1} \sum_{j=i+1}^N c_i c_j u(x_i) u(x_j) r(x_i, x_j) \quad (2.8)$$

where c_i and c_j are sensitivity coefficients of $f(x_1, x_2, \dots, x_N)$ due to the i^{th} and j^{th} variables respectively, u are standard uncertainties, and r is the correlation coefficient between x_i and x_j . Sensitivity coefficients are the partial derivatives of $f(x_1, x_2, \dots, x_N)$ with respect to the i^{th} or j^{th} variable. They represent the change in $f(x_1, x_2, \dots, x_N)$ due to the change in x_i and weigh each uncertainty component's contribution to the combined uncertainty. The second term in Eq. 2.8 is zero for independent input quantities. Many texts to refer Eq. 2.8 as root-sum-square (RSS) or add in quadrature.^{16; 17} The GUM calls Eq. 2.8 the Law of Propagation of Uncertainty (LPU).¹⁵ It should be noted that the LPU is valid for small and symmetric uncertainties and $f(x)$ being linear.

Given that Eq. 2.4 depends on the temperature to the 4th power, higher order terms of the expansion may be needed for nonlinearity. Zhang¹⁸ provides an expression for the expectation value of a k^{th} order Taylor expansion:

$$E(y^r) = \sum_{k=0}^{\infty} \frac{1}{k!} \left(\sum_{i=1}^N \frac{u_i^2}{2} \left(\frac{\partial^2}{\partial x_i^2} \right) \right)^k [f(x_1, x_2, \dots, x_N)]^r \quad (2.9)$$

where r is the order of the moment of y . Here the x_i 's are independent and normally distributed. A formula for variance for the k^{th} Taylor series is also given by Zhang, but Eq. 2.9 is easier to implement in Mathematica[®]. Equation 2.9 can be used to obtain variance from:

$$\text{var}(y) = E(y^2) - [E(y)]^2 \quad (2.10)$$

where y^2 is the second order moment of y . Standard uncertainty is the square root of the variance.

The equations above are used in many approaches in uncertainty analysis, but combining traditional uncertainties arising from systematic and random sources has been debated. Systematic errors do not change with repeated measurements, but they may change depending on the normal value of the quantity or another predictable fashion.^{15; 17} They tend to shift the measured result away from the true value, or bias. Random errors are sources of error that vary with repeated measurement and can be described by sampling statistics. The randomness can be due to temporal, spatial, and other variations—these effects are not separable.¹⁵ Most approaches combine systematic and random uncertainty separately using Eq. 2.8. Excellent reviews on uncertainty analysis methodologies can be found in Dieck¹⁹ and Abernethy and Ringhiser.²⁰

Basically, the behavior of systematic sources gives the common view that systematic error limits vary little below their indicated values and do not change sign. This non-statistical behavior gives rise to various formulae for combining systematic and random errors. More over systematic error limits are effectively treated as 99.7% confidence intervals (some methods assume a confidence level of 95%) and random errors expressed at 95% confidence intervals of Student's t distribution. Depending on the

specific calculation for total uncertainty and dominance of systematic or random effects, the confidence level of the total uncertainty will vary somewhere between 95% to 99.7%.¹⁹ Monte Carlo simulations for combining 95% confidence intervals for small sample sizes showed that the RSS of the uncertainties had a confidence level higher than 95%.²⁰ To provide a consistent method for combining uncertainties, the GUM eliminates the use of confidence intervals in favor of standard deviations.

The GUM uses subtle and strict definitions to provide a foundation in which errors, regardless of their source, can be interpreted as random variables obeying their respective probability distributions. It should be noted that the GUM prefers to use the value of the measurand rather than the true value of the measurement, but they are used synonymously at times. The measurand is simply the quantity that is measured, but the description of this quantity includes any relevant mathematical expressions and statements of the measurement process and conditions.¹⁵ The concept of measurand means to emphasize that the measurement may have inherent limitations and that the value of the intended quantity may not constitute a complete measurement. This is all dictated by the desired accuracy in the measurement. Error is defined as the difference of the measured value of the measurand to the true value of the measurand; since the true value cannot be known, it follows the error cannot be known either.¹⁵ The GUM method avoids using the term error and concerns itself with the analysis of uncertainties. Also, the terms systematic effects and random effects are used to describe the uncertainty's influence on the measurement.

What is known is the measured value and its uncertainty. Likewise, the determination of a systematic error, or bias, is also an estimation. The GUM considers this estimation to be a correction as it compensates for the discrepancy between the measured

and reference values.¹⁵ This correction still has uncertainty either from incomplete knowledge or uncertainties in the calibration process. All corrections can do is to reduce systematic error, for instance as in like how an increased number of measurements reduces random errors. In the GUM approach, uncertainty components are classified by how their standard deviations are obtained. Type A uncertainties are determined from statistical methods on the measured data. For most measurements, the standard deviation of the mean is desired, so a Type A uncertainty is:

$$u_A = \frac{s}{\sqrt{n}} \quad (2.11)$$

where s is the standard deviation and n is the number of data points. The standard deviation is computed by:

$$s = \sqrt{\frac{1}{n-1} \sum_{i=1}^n (x_i - \bar{x})^2} \quad (2.12)$$

where x_i is specific data point and \bar{x} is the mean of the data. Type A designation is only reserved to measurement data for determining the value of the measurand. When Type A uncertainties are determined from previous data or separate testing, they are considered Type B when applied to a new measurement.²¹

Type B uncertainties are standard uncertainties determined by any information on the error source, typically the nature of the stated uncertainty and probability distribution. This process may be described as heuristic, but scientific judgement and skill need to be exercised. This information includes, but is not limited to, previous measurements, calibrations, manufacture specifications, and expert knowledge.¹⁵ As systematic effects tend to be Type B uncertainties, many people incorrectly assume that systematic errors and Type B uncertainties are the same. Standards such as the ASME PTC 19.10 2005, which

is one of the main pre-GUM methodologies, has adopted the GUM's interpretation of errors and uncertainties to coincide with the GUM. However, the ASME PTC 19.10 2005 still separates uncertainties into systematic and random uncertainties in their calculations as in earlier revisions.²² They place emphasis on engineering and design where knowing uncertainty from specified effects are important. The GUM approach focuses determine uncertainty in calibrations.

A drawback to the GUM is that confidence intervals cannot be reliably determined, since degrees of freedom are not known for Type B uncertainties. Though pre-GUM methods have issues with confidence levels, the uncertainties are still confidence intervals. JCGM 100:2008 uses coverage factors of two and three to approximate 95% or 99.7% confidence intervals, respectively. The Welch-Satterthwaite (W-S) formula approximates the effective degrees of freedom for combined uncertainties. It is valid for independent and normally disturbed uncertainties, yet the NASA-HDBK-8739.19-3 states it is an acceptable approximation for dependent errors.²³ The formula is:

$$\nu_{\text{eff}} = \frac{u_{c^*}^4}{\sum_{i=1}^N \frac{c_i^4 u_i^4}{\nu_i}} \quad (2.13)$$

where c_i , ν_i , and u_i are the sensitivity coefficient, degrees of freedom, and standard uncertainty of i^{th} uncertainty component and u_{c^*} is the combined uncertainty without correlations even if they exist. A complex expressions has been developed for the case of correlated uncertainties.²⁴

The GUM provides several recommended guidelines when reporting results of an uncertainty analysis. The following are preferred: the functional relationship between the measurand and input quantities; expressions for partial derivatives and sensitivity

coefficients for aforementioned formulas; values for the input quantities and their standard uncertainties, sensitivity coefficients, and degrees of freedom, list of covariances or correlation coefficients for input quantities, descriptions on how input uncertainties and correlations are determined, and the value of the measurand and its combined uncertainty.¹⁵ The GUM allows details for the evaluation of uncertainty calculation and uncertainty components to be omitted if they can be referenced in another published document.

CHAPTER 3

EXPERIMENTAL METHOD

3.1 Overview

The uncertainty analysis will be applied to the older of the two calorimeter emissometers where the bulk of the data from NSEI was obtained.²⁵⁻²⁹ Though the details are given in these earlier works, it is convenient to provide a detailed description of the system and methodology without referring to these publications. Sample preparation and TC connections are discussed separately. The design, equipment, and software for calorimeter will be provided in the following section. The experimental procedure will include important aspects in preparing the system for measurement and obtaining data. Surface area measurements are included in this section too.

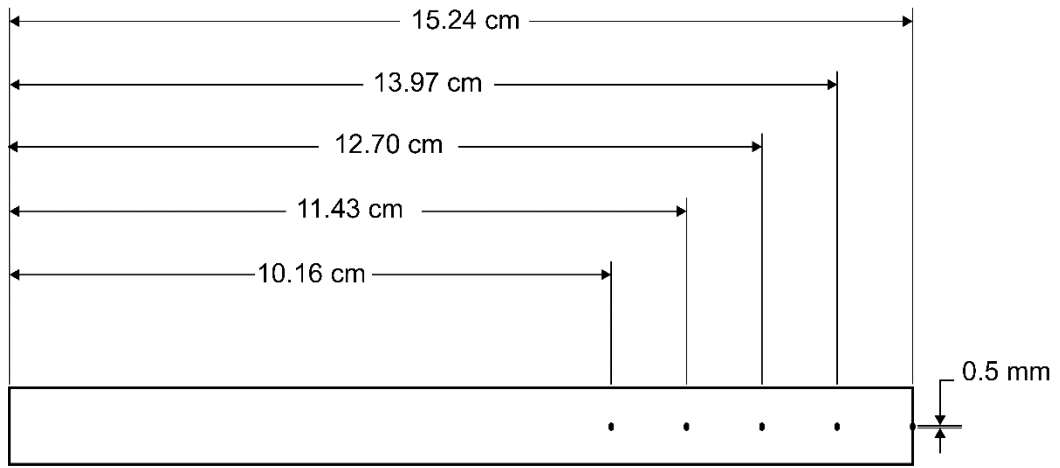
3.2 Sample Preparation

Specimens typically consist of thin rectangular strips of metal. ASTM C835-06 permits any surface condition or coating also long as it is uniform over the entire strip and compatible with a high vacuum. The size of the specimen is dictated by the its electrical resistance to the applied current to reach a desired test temperature and temperature uniformity. The placement and type of TC are also needed to measure a flat temperature while not conducting excessive heat away from the sample.

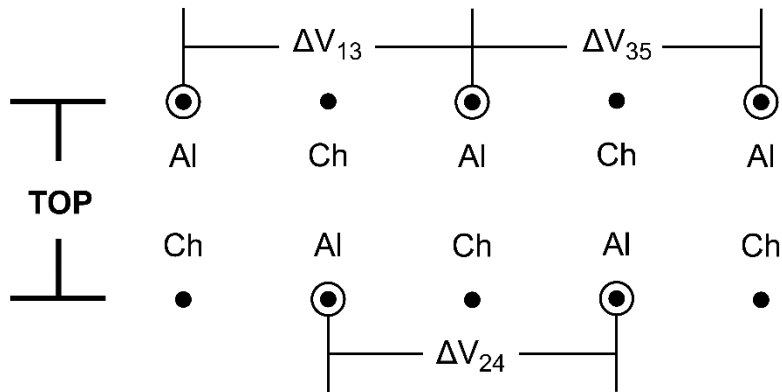
Generally, the longer the strip the flatter the temperature profile will be. This is important with Cu, Al, and their alloys that have a large thermal conductivity. ASTM C835-06 gives the example dimensions for Inconel, stainless steel, and aluminum strips for total hemispherical emissivity measurements. A thickness of 0.25 mm and width of 13 mm

are the same for all materials. Inconel and stainless steel has a total length 25 cm, but aluminum has a length of 50 cm. Thin metal strips used in studies by this group were water jet cut from sheet stock of select alloys. Water jet cutting is a computer numerically controlled process and can cut straight parallel edges as required by the ASTM C835-06. The edges were different from the main faces of the strip. Specimens were cut to a width of 1.27 cm and a length 25.4 cm at tolerances of 0.178 mm, but tolerances up to 0.125 mm are attainable with special precautions. However, alloys of interest to nuclear reactors are not readily available at any thickness. Most materials measured by this group had thicknesses from 0.254 mm to 0.635 mm, which can easily be heated up to maximum temperature with a DC current of 90 A. Hastelloy N used in a previous work had a thickness of 1.041 mm. Hastelloy N which had been oxidized for 15 minutes had the highest emissivity requiring up to 140 A to achieve the highest temperature measured—1157 K. However, the ratio of surface areas for the edges to the faces of Hastelloy N is up to 7.6%.

The measurements were determined at the central portion of the strip by at least three thermocouples (TC). The standard gives the length of the two outermost TCs as 75 mm for Inconel and stainless steel and 50 mm for aluminum. This yields a TC spacing of 38 mm and 25 mm. In this study, 5 pairs of K-type TCs are used with a spacing of 12.7 mm. The placement of the TCs was determined from one end of the strips as shown in Figure 3.1a. The TCs were spot-welded to the metal strip by the MU Physics Machine Shop. The strip was placed in a fixture that is set in a milling machine. A centering scope was used to mark the spot to be welded. The alumel and chromel leads were welded at 0.5 mm apart about the along axial centerline. Figure 3.1b shows the layout of the



(a)



(b)

Figure 3.1: (a) TC placement from the distance from one end and gap between TC leads. (b) Thermoelement layout for specimen TCs where Ch is chromel and Al is alumel. Voltage taps are on each alumel thermoelement (connected at temperature DAQ). Voltage drops are determined at each adjacent alumel lead and at additional pairs indicated above.

thermoelements for each pair. Voltage drops are measured with the alumel leads of the TCs. A voltage drop is measured for each 12.7 mm section. Sections 25.4 mm in length are measured at each end and about the center of the strip as seen in Figure 3.1b. The TC leads have an OD of 0.07 mm that was less than the 0.13 mm recommended by the standard to reduce heat loss by thermal conduction through the TC leads.

3.3 Construction of Vacuum Calorimeter

Most components of the calorimeter were commercially available hardware and equipment except for the specimen holder and TC terminal block. The specimen holder and TC terminal block were built by the machine shop on campus. Scaled drawings of the bell jar and base well are given in Figure 3.2 and Figure 3.3. Components of the DC heating circuit and equipment are shown symbolically. The vacuum chamber consisted of a stainless-steel bell jar and base well. A pulley winch setup could lift the bell jar to access the specimen holder. The connection for the bell jar and base well was sealed by the compression of an O-ring gasket. The base well includes eight 2.75 ConFlat® (CF) flanges. Six of the eight ports were in use as shown in Figure 3.3. CF flanges are ultra-high vacuum fittings. Proper installation of CF connections was done to prevent leaks.

A simple turbomolecular pump (TMP, Pfeiffer TPU-170) and rotary vane roughing pump (Welch 1376X) setup were used to achieve a high vacuum. The Pirani gauge in Figure 3.3 was used as a roughing gauge to determine when the TMP can be turned on. A cold cathode gauge was used to monitor the system pressure in a high vacuum. The O-ring gasket had a lower vacuum limit than the CF flange, but outgassing was an issue for this vacuum system as it must be opened to room air for installing samples. Since the TCs on

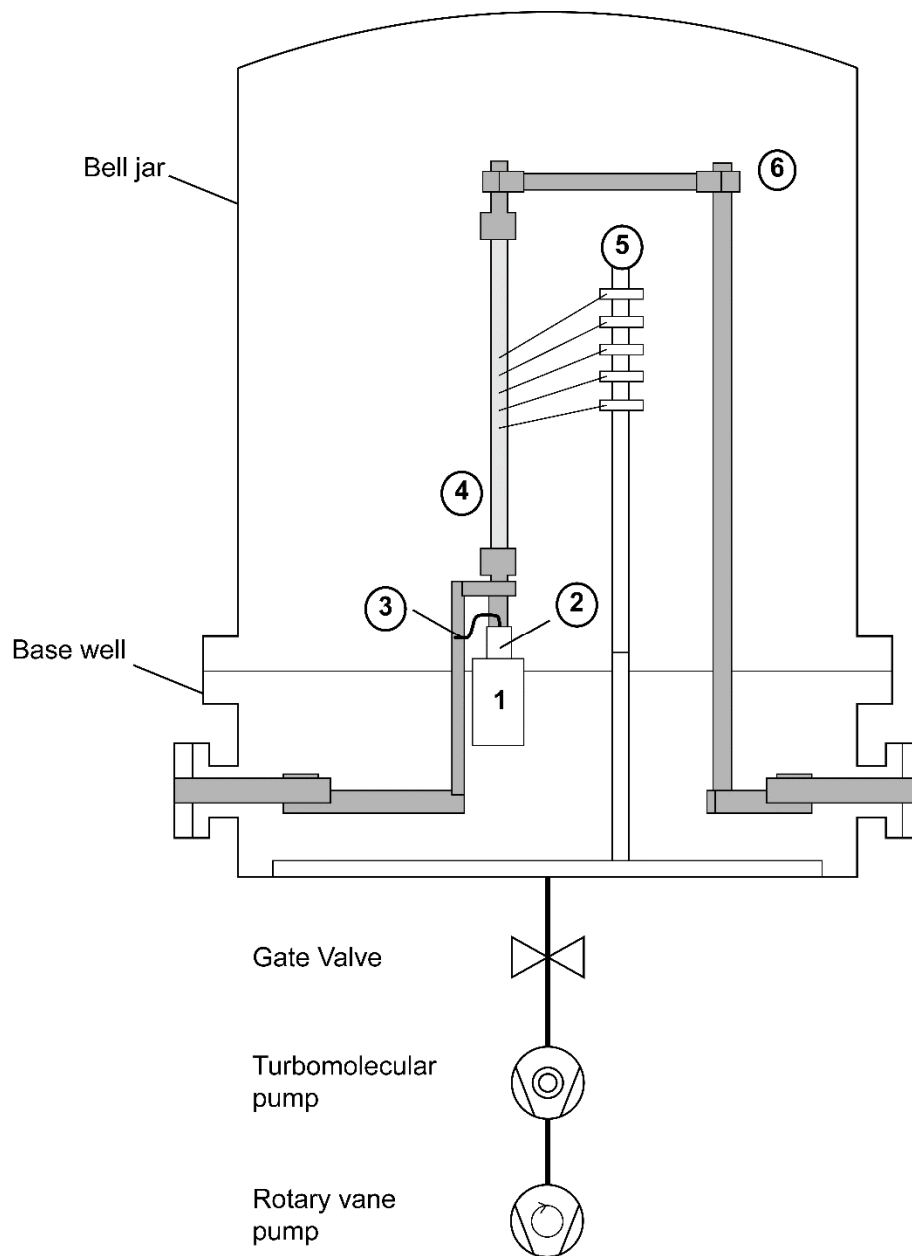


Figure 3.2: Side view of the emissometer emphasizing the specimen holder and vacuum system. The numbered labels are: (1) dead weight to prevent buckling from thermal expansion, (2) ceramic coupler to insulate specimen from dead weight, (3) low-impedance electrical cable, (4) specimen, (5) Macor® posts for connected spot-welded TCs to heavier gauge TC wire for feedthroughs, and (6) upper holder electrode that is adjustable for different length specimens.

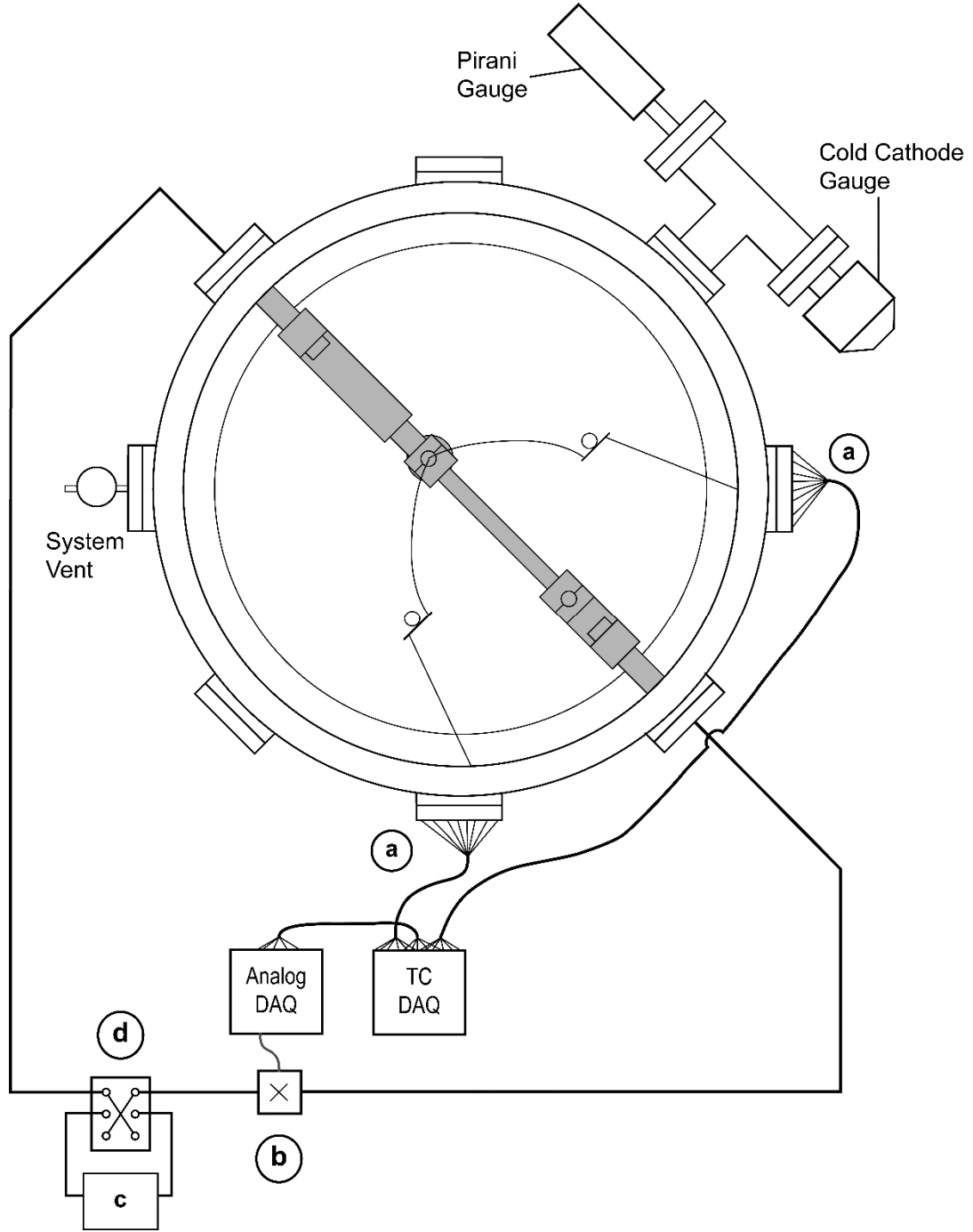


Figure 3.3: Top view of emissometer showing the layout in the base well. The labeled components are: (a) K-type TC feedthroughs, (b) hall-effect sensor, (c) DC power supply, and (d) polarity-reversing switch.

the chamber walls used a silicone adhesive and the exterior was not insulated during bake out, typical bake out temperatures could not be obtained. Experience with pumping down the system has determined an ultimate pressure of 1.3×10^{-4} Pa to 8.0×10^{-5} Pa.

The interior surface of the bell jar and base well had a height of 60 cm and a diameter of 46 cm yielding a surface area of 11,850 cm². Aremco HiE-Coat 840-M blackbody paint was applied to the interior of the bell jars as close to the manufacturer's directions as possible. The specified emissivity was at least between 0.90 to 0.95. Using the lower value of the emissivity, the right-hand side of the inequality in Eq. 2.3 gives a value of 6.2×10^{-4} for the entire surface of the strip with a thickness of 0.254 mm. In the ASTM standard, this inequality is specified over the test section surface area where the value is an order of magnitude lower. Not only was Eq. 2.3 satisfied, but the system should be adequate for measuring a high emittance material.

Specimen holders held the specimen off center in the chamber and provided the electrical connections for ohmic heating. Figures 3.2 and 3.3 show the specimen holder at two different views. They were designed to be supported by the power feedthroughs themselves. The power feedthroughs have a solid copper conductor with an OD of 1.9 cm and vacuum side length of 8.5 cm. They are rated for currents up to 600 A. The bottom holder freely moves in its support to allow thermal expansion of the specimen. A low-impedance electrical cable in Figure 3.2 provided a reliable connection from the support to the holder. A dead weight kept the specimen under tension to prevent buckling. A ceramic threaded coupler thermally insulated the holder from the dead weight. Otherwise, measurements would have taken longer to reach steady-state as the weight was heated. The top holder was firmly clamped to its support such that no wire was needed for an electrical

connection. However, the top holder could be loosened and raised or lowered for specimen lengths up to 30 cm. The sample was positioned ~ 3.5 cm off-center to reduce reabsorption of emitted radiation reflected by the chamber interior. In Figure 3.3, the DC current was provided by an HP 6671A programmable DC source. It provides up to 220 A for voltages of 0 V to 8 V. A polarity reversing switch was a double-pole double-throw knife switch that physically changed the connections between the sample holders and DC source output terminals. DC current is measured with an HTA 500-S hall effect sensor.

Specimen TCs wires were too fine to retain their shape. Heavier gauge TC wire was used to connect to the TC feedthroughs showed in Figure 3.2. The TC feedthroughs supported up to four K-type TCs each. Two self-adhesive TCs were used to take temperature on the bell jar interior. TC mounting posts consisted of a Macor[®] post screwed on top of a stainless-steel post that attached everything to the base plate. The Macor[®] rod had threaded holes for metal tabs that provide the connection between the specimen TC leads and TC extension wire. Ceramic sleeves were used to electrically insulate the TC extension wires since the wires could touch each at the feedthrough. TCs were read with the USB-TC DAQ card from Measurement Computing. Sensitivity was not specified, but the 24-bit analog-to-digital converter (ADC) for ± 80 mV gave the USB-TC a resolution of 4.8 nV. This should be adequate for the < 2 μ V sensitivity for TC electromotive force (EMF).

Data acquisition hardware was managed with a custom LabVIEW[®] virtual instrument (VI). LabVIEW[®] is a powerful graphical programming software developed by National Instruments. Measurement Computing supports easy programming of the USB-TC in a LabVIEW[®] with their own VI library. Earlier works used two separate programs

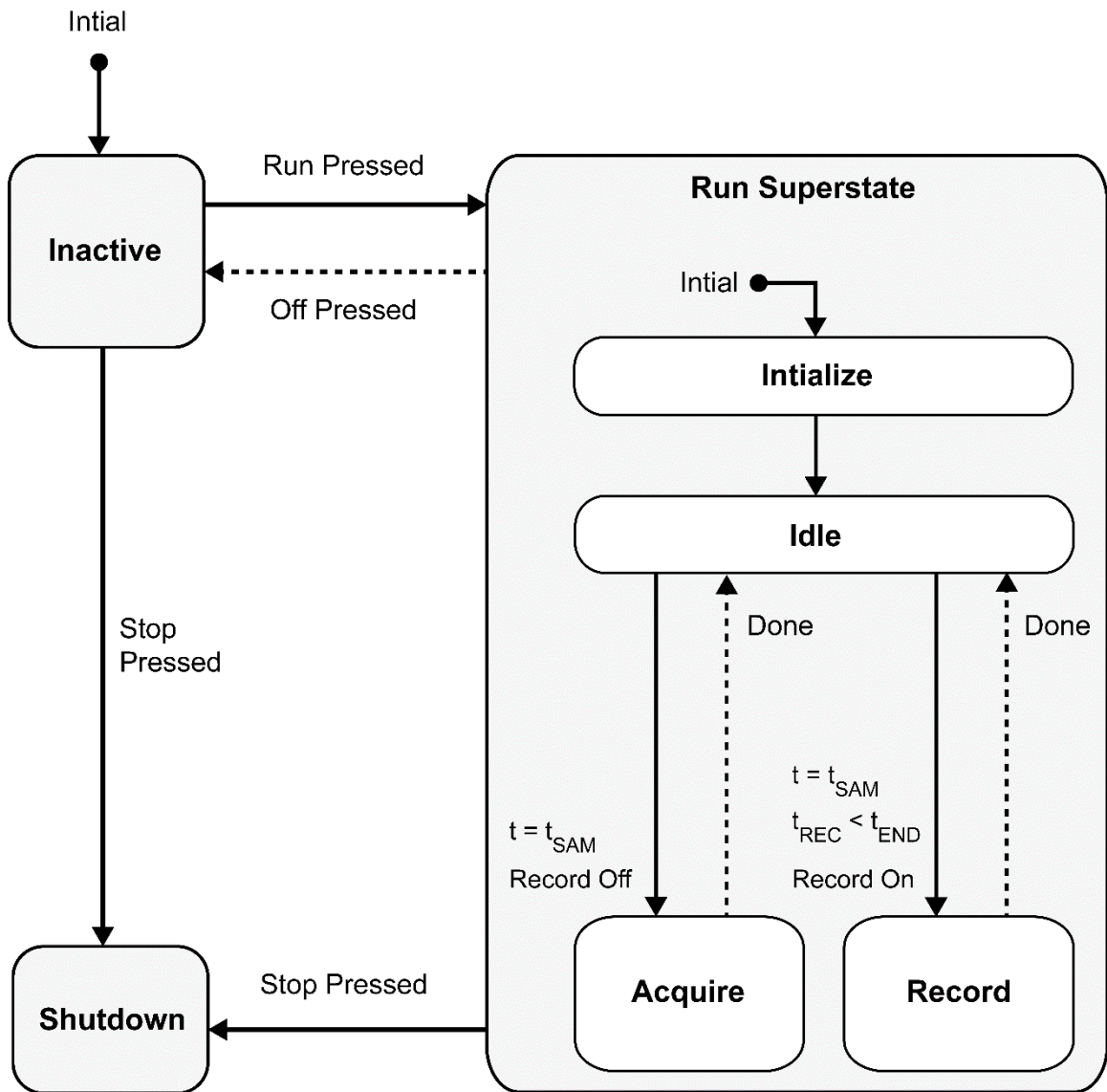


Figure 3.4: Statechart of the LabVIEW® VI for reading and recording data for calorimetric emissometers by the NSEI group. Dashed lines indicate events returning the program to a previous state.

to acquire data from the NI-USB-6251 and USB-TC separately. The two programs had to be coordinated to record data. The TraceDAQ software for the USB-TC required manual saving of files. A single VI was made to read data from both DAQ cards. No custom sub-VIs were used to prevent the VI from functioning if the sub-VI files were lost.

Basic operation of the LabVIEW® VI is given in Figure 3.4. The VI starts in an inactive state if the user wants to reconfigure the DAQ settings. By pressing Run, the program initializes the DAQ hardware and requests a file save location from the user. The program remains in an idle state until the timer counter, t , reaches the specified sample rate, t_{SAM} . The “Acquire” state reads data from the DAQ cards and displays the readings on the user interface. It also resets the timer, and triggers the “Idle” state. When the user pushes the record button, the program goes into the “Record” state where the data is read and written to a tab delimited file. The program will remain in “Record” as long as the recording time counter, t_{REC} , is less than the recording duration, t_{END} . Recording can be aborted by the user by turning off the record button.

3.4 Estimation of Non-Radiative Heat Losses and Non-grayness

Many details in this chapter are given to demonstrate the compliance of the apparatus and methods to ASTM C835-06. The standard relies on the experimenter to have the necessary background knowledge in heat transfer and the supporting literature of the ASTM C835-06. Several articles in NASA SP-31 have examined the systematic effects that reduce the amount of radiant heat loss. Fu et al.⁸ have recently compiled several of the results in NASA SP-31. ASTM C835-06 also cites the work conducted at Pratt & Whitney that contains several appendices on errors and corrections for both calorimetric and radiometric measurements in their experiments. Systematic effects include heat loss from

thermal conduction from specimen ends, thermal conduction from TC leads, gas conduction from residual gases, and non-grayness of the specimen. Figure 3.5 illustrates the heat loss mechanisms of a test section over the central region of the strip. ASTM C835-06 considers these effects negligible when following the design guidelines. The GUM states that the inclusion of systematic effects depends on their magnitude relative to the desired accuracy.¹⁵ Expressions for the systematic effects shown in Figure 3.5 from the above literature are provided here with a consistent notation. A recent data obtained on Hastelloy X with a thickness of was used in the calculations below to estimated systematic effects for the calorimeter used by the NSEL.

Thermal conduction of heat to the specimen holders can be a large source of error in determining the radiative heat. Having a longer sample as described in Section 3.2 is the best way to reduce this heat loss. But, chamber size, heating capacity of power supply, and heat dissipation of the chamber are limiting factors for long samples. When length is limited, the ASTM C835-06 has several suggestions to flatten the temperature profile such as notching the specimen (local heat generation), heating the specimen holders, or welding a low thermally conductive material to the specimen (composite specimen). The axial temperature profile can be described by the following 1-D ODE:

$$\lambda_1 \frac{d^2 T}{dx^2} + Q_1 - \frac{p\varepsilon\sigma}{A_{cs}} (T_1^4 - T_2^4) = 0 \quad (3.1)$$

where λ_1 is the thermal conductivity of the specimen in $\text{W m}^{-1} \text{K}^{-1}$, A_{cs} is the cross-sectional area in m^2 , and p is the perimeter of the specimen cross-section in m. Fu et al.⁸ integrated the Eq. 3.1 from $-L/2$ to $L/2$ to obtain:

$$Q_{\text{end-cond},\#1} = -A_{cs} \left(\lambda_1 \frac{dT}{dx} \Big|_{x=-L/2} - \lambda_1 \frac{dT}{dx} \Big|_{x=L/2} \right). \quad (3.2)$$

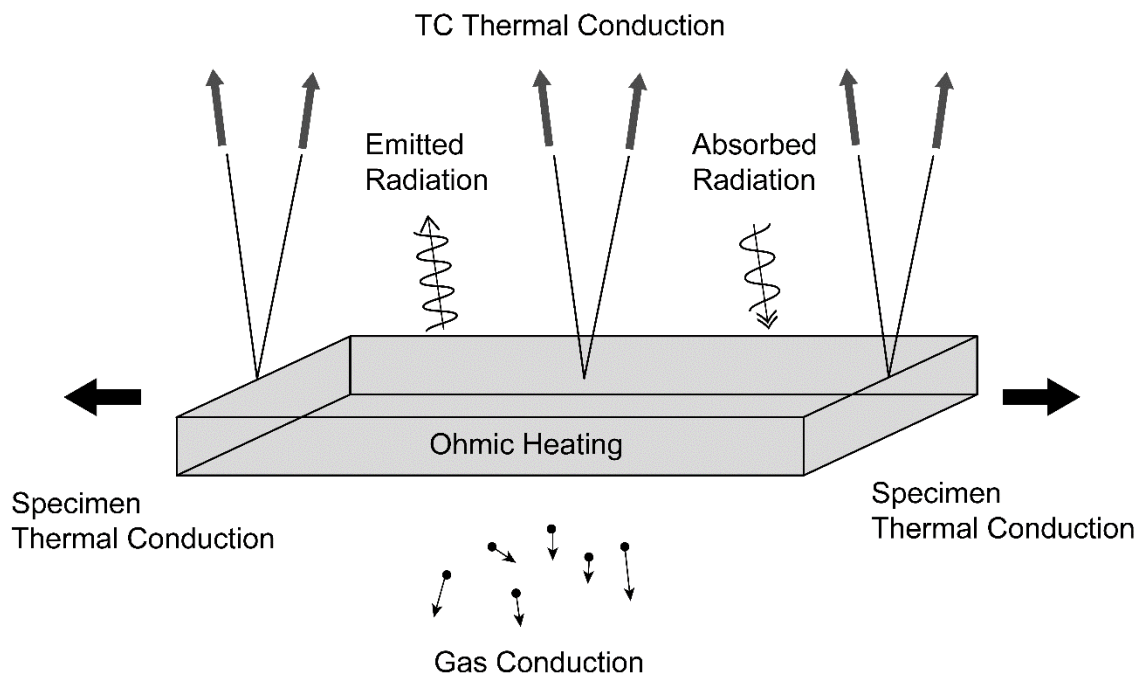


Figure 3.5: Heat loss and gain mechanisms for a test section including ohmic heating, thermal conduction in the specimen to the ends, thermal conduction in the TC leads, emitted radiation, and absorbed radiation (from chamber walls no reflection).

Here the derivatives can be approximated by slope between the adjacent TCs. The Askwyth et al.³⁰ derived a slightly different expression by considering the ideal case of the emissivity of the specimen when it is at a uniform temperature. This uniform temperature was the peak temperature at the center of the strip. The heat generated is equal to the heat radiated in the ideal case or:

$$Q_1 = -\frac{p\varepsilon_{\text{ideal}}\sigma}{A_{\text{cs}}}(T_0^4 - T_2^4) \quad (3.3)$$

where T_0 is the peak temperature of the strip in K. By substituting Eq. 3.3 into Eq. 3.1, an expression for the relative error in the emissivity to the relative error in the temperature can be derived. The solution requires non-dimensionalizing the ODE with:

$$\Theta(x) = \frac{T(x) - T_0}{T} \quad (3.4)$$

and considering small values of $\Theta(x)$ to linearize the 4th power term in the ODE. Since the heat flux and temperature are known at the center, the solution yields:

$$\frac{\Delta\varepsilon}{\varepsilon} = \frac{\varepsilon_{\text{ideal}} - \varepsilon}{\varepsilon} = 2 \left(\frac{T_0 - T(x)}{T_0} \right) \left[\left(1 - \left(\frac{T_2}{T_0} \right)^4 \right) \sinh^2(\beta x) \right]^{-1} \quad (3.5)$$

with,

$$\beta = \sqrt{\frac{\varepsilon\sigma T_0^3 p}{\lambda_1 A_{\text{cs}}}} \quad (3.6)$$

Askwyth et al.³⁰ indicated $\Theta(x)$ can vary from -0.1 to 0.1 , or $\pm 10\%$. Equation 3.5 can easily be evaluated from measured data. Most of these systematic effects are relative to the heat generated, thus the heat loss, in W, from Eq. 3.5 can be determined from:

$$Q_{\text{end-cond},\#2} = Q_1 \frac{\Delta\varepsilon}{\varepsilon}. \quad (3.7)$$

A simple expression can be used for the determination of heat conduction through the TC leads when the radiative exchange between the specimen and the TC lead are neglected. The axial temperature can be described by Eq. 3.1, but without the ohmic heating term. Gordon and London³¹ assumed the TC has a temperature of the specimen at one end and the other end approaches the temperature of the chamber wall ($x \rightarrow \infty$). The ODE can be integrated twice for:

$$Q_{\text{wire}} = \pi \sqrt{\frac{\sigma \lambda_{\text{wire}} \varepsilon_{\text{wire}} D_{\text{wire}}^3}{10} (T_1^5 - 5T_2^4 T_1 + 4T_2^5)} \quad (3.8)$$

where λ_{wire} is the thermal conductivity of the wire in $\text{W m}^{-1} \text{K}^{-1}$, $\varepsilon_{\text{wire}}$ total hemispherical emissivity of the wire (unitless), and D_{wire} is the wire's outer diameter in m. Cheng et al.³² determined a more general expression of Eq. 3.8 when the temperature of the colder end is known, but reproduces Eq. 3.8 when this end temperature is equal to the wall temperature. Thermal conductivity and emissivity for alumel and chromel (chromel-P) are available in the literature up to temperatures of 800 K and 760 K respectively. The Appendix shows data for alumel and chromel used in Eq. 3.8 in this study. As the data had a linear slope, extrapolation was used for temperatures above the reported data.

Though high-vacuum essentially eliminates convection in the calorimeter, the vacuum is not perfect and remaining gases can still obtain energy from the specimen surface leading to heat loss. At the highest temperatures measured, pressure in the chamber increased most likely due to outgassing as the temperature inside the chamber rose. The heat transfer from the specimen to the chamber wall can be described by kinetic theory. Dushman³³ gives an expression for residual gaseous conduction found in other texts^{34, 35}:

$$Q_{\text{gas}} = A_1 \alpha_r A_0 P_{\text{ccg}} \sqrt{\frac{273}{T_2}} (T_1 - T_2) \quad (3.9)$$

where α_r is the accommodation coefficient for coaxial cylinders (unitless), P_{ccg} is the cold cathode gauge reading in Pa, and A_0 is the free molecular conductivity at 273 K in $\text{W m}^{-2} \text{K}^{-1} \text{Pa}^{-1}$. For air, the free molecular conductivity is $1.23 \text{ W m}^{-2} \text{K}^{-1} \text{Pa}^{-1}$. The accommodation coefficient is a function of both the condition and temperature of specimen and chamber wall. Nelson and Bevans³⁶ and Fu et al.⁸ used an accommodation value of 1 (rough surface).

The last systematic effect concerns the specimen's absorptivity to the radiation emitted by the chamber wall. The non-grayness is expressed as:

$$\Delta\alpha = \varepsilon - \alpha . \quad (3.10)$$

For a gray body, $\Delta\alpha$ would be zero. The error from non-grayness can be calculated by:

$$\left(\frac{\Delta\varepsilon}{\varepsilon}\right)_{\text{ng},\#1} = \left(\frac{\Delta\alpha T_2^4}{\varepsilon T_1^4 - \alpha T_2^4}\right). \quad (3.11)$$

Abbott's³⁷ approach used the Hagen-Rubén approximation to create a functional relationship for emissivity, thus absorptivity, to temperature of the body:

$$\varepsilon(T) = a(\rho T)^{\frac{1}{2}} + b(\rho T) + c(\rho T)^{\frac{3}{2}} + \dots \quad (3.12)$$

where ρ is the electrical resistivity of the metal and a , b , and c are unknown coefficients³⁷.

The ratio of absorptivity to emissivity was taken at the chamber wall temperature (T_2) and specimen temperature (T_1). Since $T_1 > T_2$, only the first term in Eq. 3.12 remains:

$$\frac{\alpha}{\varepsilon} = \left(\frac{T_2}{T_1}\right)^{\frac{1}{2}} . \quad (3.13)$$

Using Eq. 3.13, the non-gray error, Eq. 3.10, becomes:

$$\left(\frac{\Delta\varepsilon}{\varepsilon}\right)_{\text{ng},\#1} = \left(\frac{T_2}{T_1}\right)^4 \left(1 - \left(\frac{T_2}{T_1}\right)^{0.5}\right) \left(1 - \left(\frac{T_2}{T_1}\right)^{4.5}\right)^{-1}. \quad (3.14)$$

Equation 3.14 is simply a function of specimen and wall temperatures. Fu et al.⁸ also used Eq. 3.13 for the calculation for total hemispherical emissivity as the absorbed radiation would be proportional to the ratio of absorptivity to emissivity. Hagen-Rubens model is applicable for polished metals for wavelengths greater than 10 μm .¹¹ Due to the low temperatures of the chamber wall, its radiation will be in the far infrared range (IR). A more general calculation for the non-gray error has been developed by Bevans and Nelson.³⁸ The spectral emissivity of the material was approximated using a black body up to a certain cutoff wavelength. There are two cases where the emissivity and absorptivity are unity from zero to the cutoff wavelength and zero above the cutoff wavelength:

$$\left(\frac{\Delta\varepsilon}{\varepsilon}\right)_{\text{ng},\#2-\text{I}} = \left(\frac{T_2^4}{T_1^4 - T_2^4}\right) \left(\frac{\int_{\lambda_c T_2}^{\lambda_c T_1} \frac{e_{\text{BB}}(\lambda T) d(\lambda T)}{\sigma T^5}}{\int_0^{\lambda_c T_1} \frac{e_{\text{BB}}(\lambda T) d(\lambda T)}{\sigma T^5}}\right) \quad (3.15)$$

and the emissivity and absorptivity are zero from zero to the cutoff wavelength and unity above the cutoff wavelength:

$$\left(\frac{\Delta\varepsilon}{\varepsilon}\right)_{\text{ng},\#2-\text{II}} = \left(\frac{T_2^4}{T_1^4 - T_2^4}\right) \left(\frac{\int_{\lambda_c T_2}^{\lambda_c T_1} \frac{e_{\text{BB}}(\lambda T) d(\lambda T)}{\sigma T^5}}{\int_{\lambda_c T_1}^{\infty} \frac{e_{\text{BB}}(\lambda T) d(\lambda T)}{\sigma T^5}}\right) \quad (3.16)$$

where the cutoff wavelength, λ_c , is in m. Unfortunately, data on metals in the far IR are scarce, especially spectral hemispherical emissivity. Del Campo et al.³⁹ obtained spectral normal emissivity up to 22 μm for select Ni-based and Co-based super alloys. Between 10 μm to 22 μm , the spectral normal emissivity decreased from 0.2 to 0.1 for brushed surfaces. The spectral normal emissivity in this range nearly doubled for sandblasted surfaces³⁹. The variation of emissivity over the temperatures 458 K and 894 K was within

± 0.25 . Calculations of spectral normal emissivities were under 0.01 for wavelengths greater than 25 μm , but these values were for room temperatures.

The corrections developed above were applied to data on Hastelloy X. Chamber pressure started to rise steadily as soon as the DC current was applied to the specimen. System pressure dropped after retesting of lower temperatures around 676 K indicating the pressure increase is due to outgassing. Equation 3.15 was used in calculating the non-grayness for Hastelloy X as the emissivity at longer wavelengths should have been negligible. The value of Eq. 3.15 dropped quickly above a wavelength of 30 μm . Thus, a cutoff wavelength of 22 μm was chosen for a conservative estimate. For emissivity at 413.6 K, conductive heat losses and non-grayness were on the order of a few percent. Askwyth's expressions for thermal conduction and Abbot's formula for non-grayness were more than the 5% accuracy stated in the standard, but the 5% value in ASTM C835-06 is also reported for the uncertainty analysis. Except for the lowest temperatures measured, the sum of all the effects were below the 5%. Above 790 K, this sum was under 1%. In addition, the lowest temperature measure was at least 120 K above the chamber wall temperature per ASTM C835-06, however both expressions for non-grayness were a few percent. Bevans and Nelson's expression can be fine-tuned when information on the spectral emissivity is available. Residual gas conduction was negligible, even when the system pressure exceeds 1.3 mPa. These calculations were done on a test section at the center of the strip with the dimensions 2.54 cm \times 1.27 cm \times 0.254 mm.

Accuracy can be improved for non-grayness, TC lead thermal conduction, and gas conduction applying the calculation of a larger area of the strip, since heat generated increases faster than these heat loss mechanisms. On the other hand, accuracy of the

Table 3.1: Calculation of systematic effects on Hastelloy X for emissivity determined between TC #2 and TC #4.

T_1	T_2	P	$Q_{I\Delta V}$	$Q_{\text{cond},\#1}/Q_{I\Delta V}$	$Q_{\text{cond},\#2}/Q_{I\Delta V}$	$Q_{\text{wire}}/Q_{I\Delta V}$	$Q_{\text{gas}}/Q_{I\Delta V}$	$Q_{\text{ng},1}/Q_{I\Delta V}$	$Q_{\text{ng},2-I}/Q_{I\Delta V}$
K	K	Pa	W	%	%	%	%	%	%
413.6	297.4	3.9×10^{-4}	0.140	1.85	7.17	2.08	0.02	5.26	3.55
541.9	297.8	4.1×10^{-4}	0.575	1.16	2.42	1.44	0.01	2.53	1.34
644.4	298.8	4.4×10^{-4}	1.314	0.8613	1.581	1.103	0.0090	1.523	0.7031
731.5	300.0	4.8×10^{-4}	2.359	0.3638	1.283	0.9177	0.0068	1.036	0.4367
790.4	301.3	5.1×10^{-4}	3.352	0.3366	1.066	0.8232	0.0057	0.8187	0.3267
826.1	302.8	5.7×10^{-4}	4.121	0.2692	0.9079	0.7686	0.0056	0.7204	0.2778
877.1	305.7	7.5×10^{-4}	5.422	0.2310	0.7568	0.7025	0.0060	0.6098	0.2238
908.0	307.5	8.5×10^{-4}	6.350	0.2263	0.7283	0.6668	0.0062	0.5541	0.1976
938.9	309.5	9.7×10^{-4}	7.384	0.1836	0.5811	0.6351	0.0063	0.5061	0.1754
979.6	315.0	1.3×10^{-3}	9.064	0.4133	0.5403	0.5893	0.0069	0.4656	0.1532
1020.7	314.3	1.3×10^{-3}	10.91	0.1535	0.4558	0.5551	0.0065	0.4112	0.1314
1060.1	319.7	2.0×10^{-3}	12.91	0.1450	0.4197	0.5271	0.0086	0.3746	0.1154
1085.3	323.3	3.1×10^{-3}	14.37	0.1417	0.4006	0.5097	0.0121	0.3592	0.1072
1118.5	329.5	4.5×10^{-3}	15.91	0.1679	0.4664	0.5061	0.0166	0.3458	0.0983
1149.3	332.0	5.2×10^{-3}	17.55	0.1292	0.3535	0.4995	0.0178	0.3234	0.0896

thermal conduction through the specimen end will diminish, because the presence of the temperature gradient along the sample. Though these corrections are approximate, the accuracy of the measurements near the lower limits needs to be considered. Increasing the length of the strip and cooling of the chamber walls will reduce the heat lost from specimen end thermal conduction and non-grayness respectively.

3.5 Experimental Procedure

Metal strips were rinsed with acetone followed by a rinse with deionized water. The strips were allowed to air dry. Prior to measurements, the calorimeter was prepared to achieve a high vacuum. A clean sample was loaded into the sampler holder wearing clean rubber gloves to prevent contamination. The leads from the spot-welded TCs were connected from top to bottom. Care was taken to give the fine wires some slack and not overtighten screw connections to reduce the chance of breakage of the leads. The bell jar was lowered, and rough pumping was started to achieve a vacuum of around 7 Pa to turn on the turbopump. At 1.3×10^{-2} Pa, the heating tape was turned on to outgas the chamber overnight. The following day the heating tape was turned off and the chamber to cool to room temperature. Measurements could start when the chamber pressure reaches at least 1.3×10^{-4} Pa.

The measurement process involved adjusting the current from the DC power supply and recording data when signals reached steady-state. A desired current value was entered in the DC power supply and the voltage was slowly increased until the power supply operated in constant current mode. Initially, the specimen could take up to 40 minutes to heat. When all specimen TCs were stable over several time bases, data was recorded with the LabVIEW® VI. The current output of the PSU was disabled and the polarity reversing

switch was flipped to the opposite side. The DC current was reengaged, and the temperatures were allowed to stabilize again to record data. Once data had been obtained for both directions of the current of a given magnitude, the current was increased to heat the sample to a different temperature. At higher temperatures, the current was decreased periodically to retest a previous data point to see if it was within 2% as required by ASTM C835-06.⁶

Surface area of the test section was measured separately from the calorimetric measurements. Length, thickness, and width of the test section were measured using digital calipers after heat transfer data was obtained from the calorimeter. This was done to prevent scratching and contaminating the surface before emissivity measurements. The resolution of digital calipers was 0.01 mm. Thus, the length, width, and thickness of the test section could be measured to the nearest 0.5 mm, 0.5 mm, and 0.025 mm respectively, as per ASTM C835-06. The test section could be between any two adjacent thermocouples, but the central most section for TCs #2 through #4 was preferred. To reduce bias in the thickness measurements, the welding beads from the specimen TCs were avoided. The thickness and width were measured at several points. Length was measured by visually aligning the jaws for the caliper next to the weld beads of the TCs.

CHAPTER 4

UNCERTAINTY ANALYSIS

4.1 Overview

The preceding chapters have given sufficient details of the measurement issues for development of the uncertainty analysis. Here the method of calculating the uncertainty in emissivity measurements is developed. Most examples of the GUM analyses are simple enough that all the required information is provided in a single table (uncertainty budget) with a description of how they were evaluated, and formulas used in computing the uncertainty. The complexity of calorimetric emissometer measurement will require its uncertainty analysis to be discussed in several steps.

The uncertainty analysis will be broken into the measurement model, sources of error, and the evaluation of uncertainty. The measurement model outlines the calculations involved to determining the emissivity from the raw data from the calorimeter. It will also describe the process of measuring currents, since it consists of a sequence of components. The next section lists the sources of error in the instrumentation and thermocouples and describes how their standard uncertainties are obtained. The last section goes through steps of propagating the uncertainty from the measured data to the final calculation. The next chapter will present the results of the uncertainty analysis on several data sets.

4.2 Measurement Model

The measurement model provides an outline and the mathematical expressions needed to derive the formula for computing the combined uncertainty at various steps and the final results. Figure 4.1 provides a flow chart for the measurement parameters from

their respective measurement devices to the equation for total hemispherical emissivity. Physical dimensions of the test section were measured with the digital calipers. Heat transfer quantities were obtained by the calorimeter. Recalling Eq. 2.4, the total hemispherical emissivity is given by:

$$\varepsilon = \frac{Q_1}{\sigma A_1 (T_1^4 - T_2^4)} \quad (4.1)$$

The surface area of the test section is obtained from:

$$A_1 = 2L_1(t_1 + w_1) \quad (4.2)$$

where L_1 is the length between two thermocouples on the strip in m, t_1 is the thickness of the strip in m, and w_1 is the width of the strip in m.

The heat radiated was assumed to be equal to the heat generated by the applied DC current. Thus, heat radiated is obtained by Ohm's law:

$$Q_1 = I|\Delta V| \quad (4.3)$$

where I is the DC current in A and $|\Delta V|$ is the absolute value of the voltage drop across the test section in V. In the calorimeter, voltage drops were measured between each TC on the specimen or as indicated in Figure 3.1b. Equation 4.3 could be applied to any of these sections. The heat output could also be added up to determine the emissivity of a larger section. Here combining adjacent sections is recommended as they will share a common TC so the average of all the TCs would have a physical meaning. Intuitively, the uncertainty accumulates in the latter case, but the detailed analysis here shows that the relative uncertainty grows slowly. For heat loss and heat gain mechanisms that cannot be neglected, Eq. 4.3 can be generalized as follows:

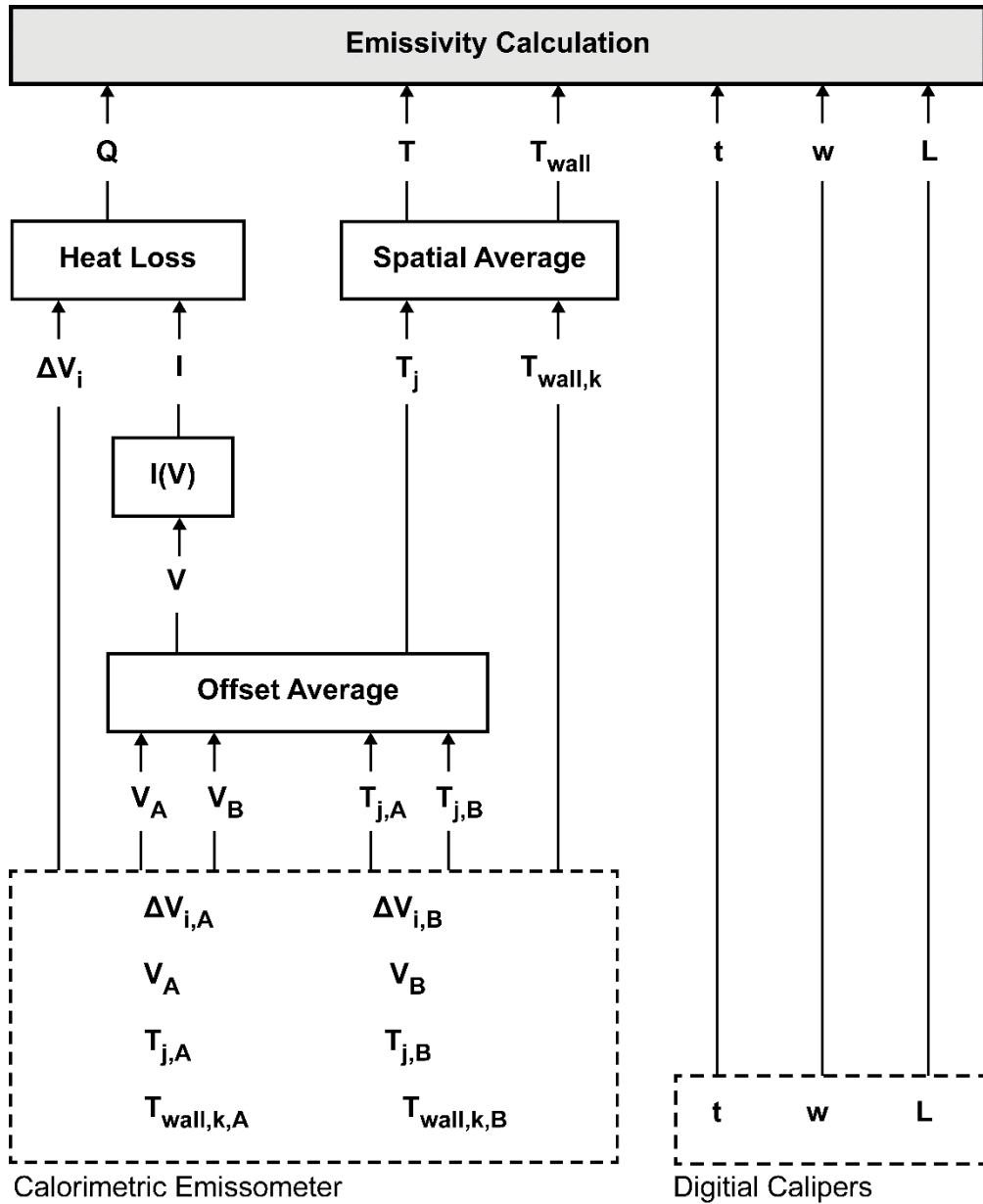


Figure 4.1: Conceptual diagram of the measurement model. Dashed boxes indicate measurement systems and their measured quantities. The indices i, j , and k indicate the number of voltage drops (total: 4), specimen temperatures (total: 5), and wall temperatures (total: 2).

$$Q_1 = I|\Delta V| + \sum_n C_n \quad (4.4)$$

where C_n represents heat loss ($C_n < 0$) or heat gain ($C_n > 0$). These corrections constitute systematic effects affecting the accuracy in determining the radiative heat loss for Eq. 4.1. Some of these corrections were estimated in Section 3.4. There will also be uncertainties for each C_n in Eq. 4.4, but were not considered in this study.

The DC current in the calorimetric measurements was not measured directly like the temperatures and voltage drops. Several devices were connected in series to convert the current to a voltage signal read by the data acquisition system (transducers). Earlier studies used a shunt resistor.^{25; 27-29} Figure 4.2a shows a schematic shunt resistor layout. The resistance of this resistor was very low (0.167 m Ω), so that the only specimen drew the current from the power supply and to minimize self-heating of the resistor. Using a different form of Ohm's law, the voltage drop across this resistor was used to determine the current (V_{shunt} in Figure 4.2a). The low resistance of the shunt produces a small V_{shunt} . A differential amplifier was needed to boost this signal (V_{out}) to be read with a DAQ device.

Later studies incorporated a Hall effect sensor (HES), LEM HTA-500-S, to eliminate excessive noise encountered in using the shunt.²⁵ A HES detects current by measuring the voltage induced on an energized metal strip due to the magnetic field emanated by a passing electrical current. This process is shown in Figure 4.2b; B_{load} is the magnetic field from current to measured. The HTA-500-S outputs a 0 V to 4 V signal that can easily be read by the DAQ card.

Regardless of the specific setup used to measure the DC current, offsets exist in the measured value. The offset in shunt resistors is caused by the Seebeck effect as heating of

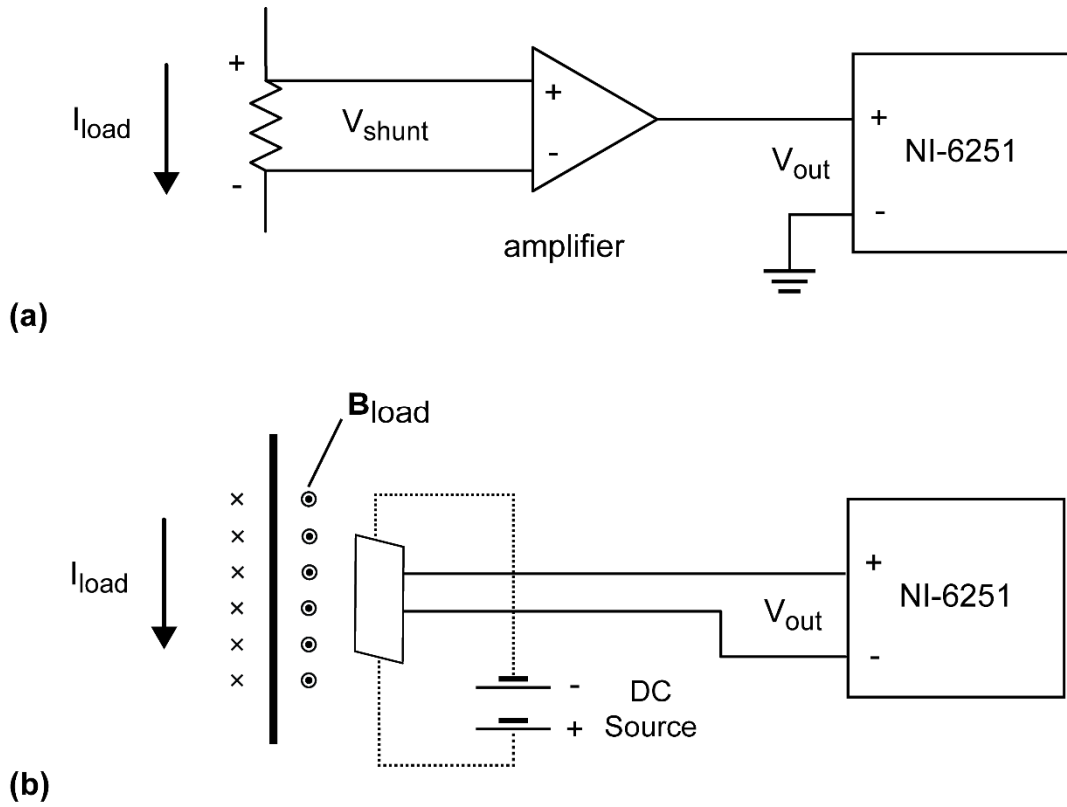


Figure 4.2: Diagrams for electrical DC current measurement sub-systems for the calorimetric emissometer built by the NSEI group: (a) shunt resistor and amplifier setup and (b) present setup consisting of HES transducer directly read by the NI-USB-6251.

the resistor or conductor causes a temperature gradient across the connections between the shunt and wire. This temperature gradient induces an EMF. For the Hall effect sensor, offsets are caused external by magnetic fields and thermal drift from heating from the measured currents. These offsets could be determined by measuring the signal when no current is applied. Ideally, this would be done periodically as the offset increases from an increase in temperature. Offsets can be eliminated by averaging readings in opposite directions:

$$V_I = \frac{|V_A| + |V_B|}{2} \quad (4.5)$$

where V_A is the voltage reading of current transducer in the positive current direction and V_B is the voltage reading in the negative current direction. One reading will have the offset added to it whereas the reading in the opposite current direction has the offset subtracted to it. For the HTA-500-S, the offset was positive so $V_A > V_I$ and $V_B < V_I$. The real motivation for averaging signal readings is to eliminate the offset for the specimen TCs.

The DC current produces an electric field through the specimen that was picked up by the specimen TCs. The alumel and chromel leads need to be perfectly aligned along the equipotential line. AC currents do not have this artifact due to the sinusoidal fluctuation of voltage, but the temperature will fluctuate with the AC power.³⁰ ATSM C835-06 mentions reversing the current to check the alignment of TCs, but there is usually some degree of misalignment. Here averaging can eliminate this offset. Unlike Eq. 4.5, the offset correction can more explicitly be written as:

$$V_{EMF} = \frac{(V_{EMF} + V_{OS}) + (V_{EMF} - V_{OS})}{2} \quad (4.6)$$

where V_{EMF} is the voltage generated through the TC circuit and V_{OS} is the offset from the voltage drop through the specimen from applied DC current. For previously measured data, the temperature DAQ was set to output temperatures rather than raw voltages. In the analysis of the old data, the offset averaging for specimen temperatures could be expressed as:

$$T_j = \frac{T_{j,A} + T_{j,B}}{2} \quad (4.7)$$

where $T_{j,A}$ and $T_{j,B}$ are the apparent temperature of the j^{th} specimen TC in the positive and negative TCs, respectively. Equation 4.7 is not preferred compared to Eq. 4.6. In practice, the EMF from the TC are converted to temperatures with the use of fitted polynomials. The inverse function for K-type TCs is given by the following polynomial:

$$t_{90} = \sum_{i=0}^9 c_i (V_{EMF})^i \quad (4.8)$$

where t_{90} is the temperature in degrees Celsius. Values of the coefficients in Eq. 4.8 are given in Table 4.1.⁴⁰ Due to the higher-order terms, the offset cannot be completely eliminated when using Eq. 4.8. Additionally, manufacturers may not use all the terms of the polynomial fit in their DAQ cards for the V_{EMF} to t_{90} .

The temperatures for the specimen and chamber wall were determined at more than one location. Two TCs were used to measure the chamber wall temperatures, while two or more TCs were used for the temperature of the test section. A spatial average was done to determine the temperatures for the specimen and chamber wall:

$$\bar{T} = \frac{1}{N} \sum_{i=1}^N T_i \quad (4.9)$$

where T_i is the temperature at the i^{th} location and N is the number of TCs.

Table 4.1: Polynomial coefficients for inverse function for K-type thermocouples.

Temperature Range (°C)	0.0–500	500–1372
Voltage Range (mV)	0.0–20.644	20.644–54.886
C_0	0.0	$-1.318\ 058 \times 10^2$
C_1	$2.508\ 355 \times 10^1$	$4.830\ 222 \times 10^1$
C_2	$7.860\ 106 \times 10^{-2}$	-1.646 031
C_3	$-2.503\ 131 \times 10^{-1}$	$5.464\ 731 \times 10^{-2}$
C_4	$8.315\ 270 \times 10^{-2}$	$-9.650\ 715 \times 10^{-4}$
C_5	$-1.228\ 034 \times 10^{-2}$	$8.802\ 193 \times 10^{-6}$
C_6	$9.804\ 036 \times 10^{-4}$	$-3.110\ 810 \times 10^{-8}$
C_7	$-4.413\ 030 \times 10^{-5}$	—
C_8	$1.057\ 734 \times 10^{-6}$	—
C_9	$-1.052\ 755 \times 10^{-8}$	—

4.3 Sources of Error

Errors arise in the measurement instruments and the measurement process itself. Measurement process errors may require calibration, special testing, and interlaboratory testing to be characterized. The focus on this study is uncertainty in the instrumentation and how it propagates through the various calculations to the measurand. This will provide the basis for adding uncertainties due to the methodology as experience is gained. Error and performance specifications for instruments can be quite ambiguous to obtain standard uncertainties for uncertainty propagation. Statistical details of error specifications are not readily available even to application specialists or technical personnel of the instrument's manufacture. It appears that for some products or brands such information may not be determined. Specifications tend to state some form of typical or maximum dispersion in an

error source. Additionally, maximum errors maybe calculated over the worst environmental conditions for the device.

The next step in the analysis was to identify the sources of error and to assign a probability distribution and confidence levels. Since most processes follow a normal distribution, a 95% confidence interval of a normal distribution is the default choice when there is no available information. Dispersions of error sources that are completely contained (100%) within specified bounds constitute a large class of distributions. In this case, rectangular distribution is a conservative assumption in the absence of any information. JCGM 100:2008 does provide some general guidance on determining the probability distributions, but the NASA-HDBK-8739.19-3 is a much better resource. For this analysis, containment limits and containment probabilities were used to describe unevaluated error limits as these limits may be tolerances, confidence intervals... etc.²³ When containment limits are provided in this work without a containment probability, the containment limits are an expanded uncertainties due to a coverage factor instead of a confidence interval. Standard uncertainties for Type A errors were calculated from the data set and containment limits and probability were not needed.

Dimensional measurements for the test section are subjected to errors in the instruments and correlations from the measurement process. Table 4.2 shows the containment limit error sources and the needed information to determine their standard uncertainties. The digital calipers conformed to the DIN 862 standard. For lengths up to 100 mm, the DIN 862 states an MPE is 20 μm for digital calibers for lengths up to 100 mm (3.94 inches). DIN 862 does not give a confidence level for the MPE, but it does specify the MPE is not a symmetrical value i.e. $\pm 20 \mu\text{m}$.⁴¹ A one-sided normal distribution was

assumed with a 95% confidence level. Saecker and Klinke⁴² examined the uncertainty in manual versus automatic calibration of calipers. Their testing indicated that variations in force applied to calipers can give an error of $\pm 15 \mu\text{m}$, which is normally distributed with a coverage factor of 2. They noted that even trained users tend to vary pressure when calipers were slightly off from the expected result. Containment limits of caliper resolution was 1/2 of the least significant digit of resolution following a rectangular distribution. Physical dimensions should be repeated several times to determine an average value, but it was not considered in this study.

Table 4.2: Errors sources for dimensional measurement devices.

Error Source	Error Type	Containment		Probability Distribution	Divisor	D.O.F.
		Limits	Probability			
Digital Calipers						
MPE	B	20 μm	95%	Normal (one-sided)	1.64	∞
Operator Bias	B	15 μm		Normal	2	∞
Resolution	B	5 μm	100%	Rectangular	$\sqrt{3}$	∞

All the electrical signals from the calorimeter were analog differential voltages. TC signals were converted to temperatures by the DAQ, so the errors from those measurements will be discussed separately. National Instruments uses the term Absolute Accuracy to specify the uncertainty in most of their devices. This accuracy depends on the voltage range the device is setup to measure, called full scale (FS), and the value of the voltage. The absolute accuracy is calculated from:

$$AA = G_{\text{err}} \text{RDG} + (\text{OS}_{\text{err}} + 6 \times 10^{-5}) \text{FS} \quad (4.10)$$

where RDG is the reading in V, G_{err} is coefficient for the gain error and OS_{err} is the

coefficient for the offset error. Values for the G_{err} and OS_{err} for the NI-USB-6241 due to channel full scale setting are given in Table 4.3. The INL Error was given explicitly in Eq. 4.10 as it is the same for all settings. The NI-USB-6251 analog voltage channels were all set to ± 10 V range in data published by the NSEI group.²⁵⁻²⁹ In Chapter 5, an examination of the absolute accuracy for millivolt signals will show larger uncertainty from the NI-USB-6251 in then ± 10 V range setting compared to more appropriate range settings.

Table 4.3: Values for resolution and gain and offset errors for the NI-USB-625.

Nominal Range (FS)	Resolution	Gain Error	Offset Error
V	μV	ppm/RDG	ppm/FS
± 10	310	60	20
± 5	200	70	20
± 2	60	70	20
± 1	30	80	20
± 0.5	20	90	40
± 0.2	6	130	80
± 0.1	3	150	150

The voltage drops for the test section were measured where the alumel leads connected to the temperature DAQ. When two DAQ cards are connected in this fashion cross-talk can be another source of error. This cross-talk can either alter readings or add noise to the signal. Table 4.4 shows data from a simple cross-talk test on the NI-USB-6251. The cross-talk test consisted of comparing the average readings and standard uncertainties from the NI-USB-6251 when the tapped alumel leads were connected then disconnected from the USB-TC temperature DAQ. No test was attempted for cross-talk in the USB-TC

due to the NI-USB-6251. There appeared to be slightly less noise with the voltage taps disconnected from the USB-TC, but the mean values and the spread of voltage signals were consistent to 1 mV. In addition, the TC wires and voltage taps wires were not twisted shielded pairs, so there could have been other causes for the change in noise. Cross-talk would need to be determined for a variety of conditions, thus cross-talk was neglected.

Table 4.4: Cross-test test on a Hastelloy X strip at -30 A for NI-USB-6251.

Voltage	Connected	Disconnected
V	mV	mV
TC #1 to TC #2	-138.99 ± 1.35	-139.17 ± 0.97
TC #2 to TC #3	-140.79 ± 1.02	-141.10 ± 0.78
TC #3 to TC #4	-142.23 ± 1.20	-142.51 ± 1.04
TC #4 to TC #5	-139.90 ± 1.35	-140.14 ± 1.00
TC #1 to TC #3	-280.50 ± 1.01	-280.96 ± 0.72
TC #2 to TC #4	-283.83 ± 1.08	-284.34 ± 0.79
TC #3 to TC #5	-282.82 ± 1.41	-283.37 ± 1.26

Sources of error in the voltage measurements were mostly from the DAQ error and error from repeated measurements. Table 4.5 summarizes the errors sources for measuring analog voltage signals. From the example calculation, the noise of a DAQ device was multiplied by a coverage factor of 3. Based on NI's use of noise in the AA calculations, the AA appeared an expanded uncertainty with a coverage factor of 3. Per National Instruments recommendations, the noise was not included in the calculation of AA for repeated measurements, which occurs in the emissivity measurements.⁴³ Random errors like noise were considered separately and were obtained using Eqs. 2.11 and 2.12. The

repeatability of NI-USB-6251 has two degrees of freedom, since voltage drops and voltage reading from the HES were combined differently. Voltage drops only changed in sign when the direction of the DC current was reversed. The absolute values of the voltage drops were combined into single data sets. The voltage readings from the HES changed in magnitude due to the presence of an offset as discussed in Section 4.1. Voltage signals from the HES were averaged per Eq. 4.5 and the degrees of freedom were determined by the W-S formula. Resolution error in the NI-USB-6251 came from the ADC. Containment limits for resolution in a DAQ card were determined by dividing the full-scale range by two raised to the power of one plus the ADC resolution in bits. The NI-USB-6251 features a 16-bit ADC. Resolution error in a DAQ card also follows a rectangular distribution.²³

Table 4.5: Errors sources for the NI-USB-6251.

Error Source	Error Type	Containment		Probability Distribution	Divisor	D.O.F.
		Limits	Probability			
Absolute Accuracy	B	Eq. 4.10	—	Normal	3	∞
Resolution	B	$FS/2^{17}$	100%	Rectangular	$\sqrt{3}$	∞
Repeatability	A				1	79 159

Errors in the temperature measurements included errors in the thermocouple and data acquisition hardware. Table 4.6 lists the error sources in the TC and USB-TC. ASTM C835-06 requires calibration of the specimen TCs, but researchers who have used calorimeters like or compliant to the ASTM C835-06 have not provided any details of such calibrations. TC calibration involves comparing the TC to be tested with a reference thermometer. Depending on the temperature range, the reference thermometer could be a RTD or a calibrated TC. Green et al.⁴⁴ examined the performance of an S-type TC spot-

welded onto a small piece of Inconel 718 to a premade S-type sheathed TC. The two TCs were heated in a furnace at atmospheric pressure. The gas is assumed to be air as this test was to assess anomalous readings of temperature and emissivity above 1273 K for oxidized Inconel 718 samples. This test can be considered a form of calibration and the results could have been corrected. However, calibrating the TCs on a specimen prior to emissivity measurements presents a challenge. First, spatial temperature uniformity of the furnace and bath need to be adequate over a large region due to the size of the specimens. Another issue is ensuring the specimen surfaces are not altered during the TC calibration process. Spot-welded TCs can be calibrated after measurement by cutting the portions with the TCs and calibrating each TC separately though TCs may drift over during the measurement due to their fine diameter and the large temperature gradient during emissivity measurements.

Inhomogeneities also constitute another source of error in TC thermometers. A specialized test is done to measure the Seebeck coefficient along the TC wire used. It is the change of the Seebeck coefficient along the TC wires that created drift in the measurement. The changes caused by various physical and chemical processes can be unique to specific TC types.⁴⁵ A common method involves inserting a TC in a uniform bath or furnace in fixed increments and measuring the V_{EMF} as a function depth. Furnaces usually require cooling where the TC is inserted to create a steep temperature gradient to generate the EMF. A reference thermometer is also used along with TC to be tested since furnaces do not have the uniformity of liquid baths.⁴⁶ Without any calibration data or Seebeck coefficient of specimen TCs, TC tolerances for K-type thermocouples were used as an estimate of inherent TC error. The standard tolerance in the temperature range 0°C to 1260°C for K-type TCs is:

$$\max(\pm 2.2 \text{ }^\circ\text{C}, 0.0075 T) \quad (4.11)$$

where T is the nominal value of temperature in $^\circ\text{C}$.⁴⁰ These tolerances are applicable only to new TC wire. Specimen TCs were not re-used in emissivity measurements. Thus, their tolerances would obey Eq. 4.11. The self-adhesive TCs used to measure the bell jar temperatures were not regularly replaced. However, they were not exposed to extreme conditions to cause substantial drift. Bently⁴⁷ notes that such tolerances are for the rejection of failed TCs rather than an indication of actual performance. The TC standard tolerance was treated as the containment limits for a rectangular distribution.

Table 4.6: Errors sources for K-type TCs and temperature DAQ.

Error Source	Error Type	Containment		Probability Distribution	Divisor	D.O.F.
		Limits	Probability			
K-type Thermocouple						
Inherent Error	B	Eq. 4.11	100%	Rectangular	$\sqrt{3}$	∞
USB-TC						
Maximum Error	B	0.691 $^\circ\text{C}$	95%	Normal	1.96	∞
Resolution	B	$1.2 \times 10^{-4} \text{ }^\circ\text{C}$	95%	Normal	1.96	∞
Repeatability	A					79 159

The USB-TC data acquisition card had both an accuracy and resolution error. The manual for the USB-TC reported a typical and maximum errors that were combined from linearization, cold-junction compensation, and system noise error sources.⁴⁸ Combined errors can be considered normally distributed due the Central Limit Theorem. The stated maximum error values were not multiples of typical error values and appear to be worst

case error for the USB-TC in a harsh environment. USB-TC typical error was used in this analysis. A confidence level of 95% was chosen as no other information was available. The resolution error of the USB-TC comes from 24-bit ADC for a full-scale range of ± 80 mV. The resolution for USB-TC needed to be converted to a temperature for this analysis. The resolution in degrees Celsius using K-type TCs was obtained by evaluating Eq. 4.8 for the specified resolution in volts. Its value is given in Table 4.6. Finally, the temperature measurements would also have a repeatability error.

A transfer function was is for the propagation of uncertainty in the DC current measurements as it involves a sequence of devices from the source to the readout. For the LEM HTA-500-S, the transfer function is:

$$V_{\text{HES}} = S(I_{\text{SP}} + e_{\text{ACC}} + e_{\text{LIN}}) \quad (4.12)$$

where V_{HES} is the voltage output in V, I_{SP} is the measured current from the DC source in A, S is the conversion factor in V A^{-1} , e_{ACC} is the accuracy in A, and e_{LIN} is the linearity in A. The last two parameters are dummy variables, so that the LPU can be applied to Eq. 4.12. They have a nominal value of zero, since the device should be compensated for these effects. Table 4.7 gives error sources of the HTA-500-S. LEM specifications state that the max error is 99.7% confidence interval of a normal distribution.

The uncertainty in I_{SP} was due to the total uncertainty in the power supply. The DC power supply has several sources of error. Programming accuracy refers to how the close the power supply can output the current to the specified user set point. The readback accuracy is how well the power supply can monitor the supplied current. Load and line regulations is how much the output changes when the load and AC wall power change. Each of these sources have a gain and offset component in the containment limits.

Table 4.7: A list of error sources for the DC power supply unit and HES transducer.

Error Source	Error Type	Containment		Probability Distribution	Divisor	D.O.F.
		Limits	Probability			
Hall Effect Sensor: LEM HTA 500-S						
Accuracy	B	±5 A	99.7%	Normal	3	∞
Linearity	B	±2.5 A	99.7%	Normal	3	∞
DC Current Source: HP 6671A						
Programming Accuracy	B	±(0.1% RGD + 0.125) [A]	95%	Normal	1.96	∞
Readback Accuracy	B	±(0.1% RGD + 0.150) [A]	95%	Normal	1.96	∞
Load Regulation	B	±(0.005% RGD + 0.0010) [A]	95%	Normal	1.96	∞
Line Regulation	B	±(0.005% RGD + 0.0010) [A]	95%	Normal	1.96	∞
Ripple & Noise	B	0.200 [A]	95%	Normal	1.96	∞
Resolution	B	0.0275 [A]	100%	Rectangular	$\sqrt{3}$	∞

Keysight technical support verified these specifications are 95% confidence intervals of a normal distribution.⁴⁹ For proper bookkeeping, a transfer function is required for the NI-USB-6251 reading of the HTA 500-S output. The transfer function is:

$$V_{6251} = V_{\text{HES}} + AA(V_{\text{HES}}) + e_{6251,\text{RES}} + e_{6251,\text{RAN}} \quad (4.13)$$

where V_{HES} is the output voltage of the HES in V, AA is the absolute accuracy of the NI-USB-6521 in V, $e_{6251,\text{RES}}$ is the resolution of NI-6251 in V, and $e_{6251,\text{RAN}}$ is the random uncertainty from repeatability. Again, $AA(V_{\text{HES}})$, $e_{6251,\text{RES}}$, and $e_{6251,\text{RAN}}$ are dummy variables for the uncertainty propagation. AA and $e_{6251,\text{RES}}$ are zero as they are compensated, but $e_{6251,\text{RAN}}$ is zero as the expectation values of random errors are zero.¹⁵

4.4 Calculation of Uncertainties

The measurement model for the emissivity measurements was discussed from the top down. Uncertainties were calculated for the measured data and propagated through intermediate calculations to the emissivity calculation. Measurements for physical dimensions, temperatures, and voltage drops were considered direct measurements. Since all errors are random variables under the GUM method, the LPU can be rigorously defined for a direct measurement.²³ The measurement model for a direct measurement is:

$$x = x_{\text{true}} + \sum_{k=1}^N e_k \quad (4.14)$$

where x_{true} is the true value of quantity x , e_k is the k^{th} error source, and N is the total number of error sources. Taking the variance of Eq. 4.14 gives:

$$\begin{aligned} \text{var}(x) &= \text{var} \left(x_{\text{true}} + \sum_{k=1}^N e_k \right) \\ &= \text{var} \left(\sum_{k=1}^N e_k \right) \\ &= \sum_{k=1}^N u_k^2 + 2 \sum_{k=1}^{N-1} \sum_{j=k+1}^N \rho_{k,j} u_k u_j \end{aligned} \quad (4.15)$$

where u are standard uncertainties and ρ is the correlation coefficient. The variance of x_{true} is zero as it is an exact quantity. The second term on the right side of Eq. 4.15 is zero when u 's are independent. Equation 4.15 is quite similar to Eq. 2.8, but without the sensitivity coefficients. For instruments, error specifications are given in the same unit, but some may need to be converted. The uncertainty in the caliper measurements will be the same of all dimensions, thus:

$$u_X^2 = u_{X,ACC}^2 + u_{X,OP}^2 + u_{X,RES}^2 \quad (4.16)$$

where $u_{X,ACC}$ is standard uncertainty from accuracy per DIN 862 in m, $u_{X,OP}$ is the standard uncertainty due to operator error in m, and $u_{X,RES}$ is the standard uncertainty from the caliper resolution in m. All temperatures measured have a standard uncertainty of:

$$u_T^2(T) = u_{K-type}^2(T) + u_{USB-TC,ACC}^2 + u_{USB-TC,RES}^2 + u_{T,RAN}^2 \quad (4.17)$$

where T is the temperature in °C, u_{K-type} is standard uncertainty from K-type TC tolerance in °C, $u_{USB-TC,ACC}$ is the standard uncertainty from USB-TC accuracy in °C, $u_{USB-TC,RES}$ is the standard uncertainty from the USB-TC resolution in °C, and $u_{T,RAN}$ is the standard uncertainty from repeated measurements in °C. The error in the TC itself is the only term dependent on the value of temperature. Voltage drops between the specimen TCs have a:

$$u_{\Delta V}^2(\Delta V) = u_{6251,AA}^2(\Delta V) + u_{6251,RES}^2 + u_{\Delta V,RAN}^2 \quad (4.18)$$

where ΔV is the average voltage drop in V, $u_{6251,AA}$ is standard uncertainty from Eq.4.10 in V, $u_{6251,RES}$ is the standard uncertainty from NI-USB-6251 resolution in V, and $u_{\Delta V,RAN}$ is the standard uncertainty from repeated measurements in V.

The standard uncertainty for the DC current needed to be determined at the source and propagated through the transfer functions of DC current measurement sub-system. The DC power supply had a combined standard uncertainty analogous to a direct measurement where the components were added in RSS:

$$u_{I,SP}^2(I) = u_{6671A,PA}^2(I) + u_{6671A,RA}^2(I) + u_{6671A,LLR}^2(I) \quad (4.19)$$

$$+ u_{6671A,RN}^2 + u_{6671A,RES}^2$$

where $u_{6671A,PA}$ is standard uncertainty from programming accuracy in A, $u_{6671A,RA}$ is the standard uncertainty from readback accuracy in A, $u_{6671A,LLR}$ is the standard uncertainty from line and load regulation in A, $u_{6671A,RN}$ is the standard uncertainty from ripple and noise in A, and $u_{6671A,RES}$ is the standard uncertainty from programming resolution in A. All sources above had infinite degrees of freedom, thus effective degrees of freedom was infinity for u_I . W-S formula was valid for the DC current source as u_I is dominated by normally distributed uncertainties from a Type B evaluation.¹⁵ This uncertainty adds to the uncertainty of the HES. Using the LPU on Eq. 4.12 and noting the sensitivity coefficients for all the variables is S , standard uncertainty for the HES is given by:

$$u_{V,HES}^2 = S^2 \times (u_{I,SP}^2 + u_{ACC}^2 + u_{LIN}^2) \quad (4.20)$$

where $u_{I,SP}$ is standard uncertainty from the power supply in V, u_{ACC} is the standard uncertainty of HES's accuracy in V, and u_{LIN} is the standard uncertainty in HES's linearity in V. Finally applying LPU to Eq. 4.13 gives the total standard uncertainty in the DC current measurements from the NI-USB-6251:

$$u_{V,6251}^2(V_{HES}) = u_{V,HES}^2(V_{HES}) + u_{6251,AA}^2(V_{HES}) \quad (4.21)$$

$$+ u_{6251,RES}^2 + u_{V,RAN}^2$$

where $u_{V,RAN}$ is the standard uncertainty from repeated measurements in V.

Uncertainty propagation is different for the offset and spatial averaging. The offset averaging for the voltage reading for DC current (Eq. 4.5) and specimen temperature

(Eq. 4.7) are straightforward for uncertainty propagation. The sensitivity coefficient of any of the variables was one half. The uncertainty in the voltage for DC current is:

$$u_V^2 = \frac{u_{V,6251}^2(V_A) + u_{V,6251}^2(V_B)}{4} \quad (4.22)$$

where V_A and V_B is the voltage readings in V for the positive and negative DC current directions, respectively. The ohmic heating Eq. 4.22 needs to be expressed in A. The final uncertainty in the DC current is:

$$u_I^2 = c_{S,Inv}^2 u_V^2 \quad (4.23)$$

where $c_{S,Inv}$ is the reciprocal of the HES conversion factor S . Its value was 125 A V^{-1} . Since all sources of uncertainty were incorporated into u_V , Eq. 4.23 is merely a unit conversion. The uncertainty for j^{th} specimen TC is given by:

$$u_{T,j}^2 = \frac{u_{T,j,A}^2 + u_{T,j,B}^2}{4} \quad (4.24)$$

where $T_{j,A}$ and $T_{j,B}$ is the temperature readings in K for the positive and negative DC current directions, respectively. Spatial averages were slightly different than offset averages. In addition to the uncertainty from each T_j , the standard deviation between the spatial average and temperatures at each j^{th} location is a measure of the uncertainty due to the non-uniformity that cannot be determined from the having sufficient number of probes.^{16; 22} Uncertainty in the spatial average in temperatures is:

$$u_{T,j}^2 = \sum_{k=1}^{N_T} \frac{u_{T,k}^2}{N_T^2} + \sum_{k=1}^{N_T} \frac{(T_k - \bar{T})^2}{N_T(N_T - 1)} \quad (4.25)$$

where N_T is the number of locations, $u_{T,k}$ is obtained from either Eq.4.23 for specimen TCs or Eq. 4.17 for wall TCs. The $N - 1$ in the denotator of the second term is the degrees

of freedom for determining the standard deviation between the spatial average and T_k . The N is to convert the standard deviation into the standard deviation of the mean. When accounting for only the uncertainty for repeatability, the first term on the right-hand side is the same for the pooled standard deviation in Figliola's and Beasley's uncertainty analysis for the temperature distribution in an oven.¹⁶ It represents the inseparable spatial and temporal variation of each T_k to T .

Finally, the uncertainty in the emissivity can be determined with the uncertainty propagation heat generated and the Stefan-Boltzmann equation. The last intermediate calculation is the uncertainty in the heat generated. Equation 4.1 could be expressed in I and $|\Delta V|$, but keeping Q_1 separate allows the corrections from Section 3.4 to be incorporated if needed. Uncertainty for Eq. 4.4, without corrections, is given by:

$$u_{Q_1}^2 = (\Delta V)^2 u_I^2 + I^2 u_{\Delta V}^2 \quad (4.26)$$

where u_I is uncertainty in the DC current from Eq. 4.23 in A and $u_{\Delta V}$ is uncertainty in the voltage drops in V. Substituting Eq. 4.2 into Eq. 4.1, the combined uncertainty for total hemispherical emissivity is:

$$u_\varepsilon^2 = c_{Q_1}^2 u_{Q_1}^2 + c_L^2 u_L^2 + c_t^2 u_t^2 + c_w^2 u_w^2 + c_{T_1}^2 u_{T_1}^2 + c_{T_2}^2 u_{T_2}^2 \quad (4.27)$$

where c_j and u_j sensitivity coefficients and standard uncertainties of the j^{th} input quantity. Table 4.8 lists the expressions for each sensitivity coefficient in Eq. 4.27. Emissivity is unitless so sensitivity coefficients are simply the reciprocals of units for their respective standard uncertainties. Uncertainties for L , w , and t were computed by Eq. 4.16 for each dimension. Equation 4.25 was used twice for u_{T_1} and u_{T_2} , while u_{Q_1} was from Eq. 4.26.

Table 4.8: A list of sensitivity coefficients for the combined uncertainty by Eq. 4.27.

Symbol	Expression	Unit	Equation
C_{Q_1}	$\frac{1}{2L_1(t_1 + w_1)\sigma(T_1^4 - T_2^4)}$	W^{-1}	4.28
C_{T_1}	$-\frac{2Q_1(T_1)^3}{L_1(t_1 + w_1)\sigma(T_1^4 - T_2^4)^2}$	K^{-1}	4.29
C_{T_2}	$-\frac{2Q_1(T_2)^3}{L_1(t_1 + w_1)\sigma(T_1^4 - T_2^4)^2}$	K^{-1}	4.30
C_{L_1}	$-\frac{Q_1}{2L_1^2(t_1 + w_1)\sigma(T_1^4 - T_2^4)}$	m^{-1}	4.31
C_{t_1}	$-\frac{Q_1}{2L_1(t_1 + w_1)^2\sigma(T_1^4 - T_2^4)}$	m^{-1}	4.32
C_{w_1}	$-\frac{Q_1}{2L_1(t_1 + w_1)^2\sigma(T_1^4 - T_2^4)}$	m^{-1}	4.33

CHAPTER 5

RESULTS

5.1 Overview

It is not practical to provide to all details on entire sets of data. In addition, examining the uncertainty at particular stages is more economical in assessing the performance of the measurements process. First the uncertainty in the measurement devices are examined. This will provide an understanding of the uncertainty in the measured values before being propagated through the various formula. Section 5.3 gives uncertainty budgets at the level of the emissivity calculation for select cases to estimate the contributions of input the main quantities. This also requires in examining the uncertainty budgets for ohmic heating. Error bar plots will be reported in the Section 5.4 to show trends in the uncertainty of entire data sets. Brief discussion of the results is also provided.

5.2 Instrumentation Uncertainty

The variability of electrical resistance and thermal emittance of specimens made it difficult to assess the uncertainty of the data acquisition setup over the operational range in the emissivity measurements. With the exception of repeatability errors, other sources in the instrument can be evaluated at select values that span the range of most measurements. Electrical resistance and emissivity determined the amount of amperage need to heat the specimen to given temperature. The driving voltage from the HP-6671A and electrical resistance affected the magnitude for the voltage drop between the TCs. Based on the nominal values of the temperature and voltage signals, the DAQ uncertainty will be provided over a range of values expected to occur during measurements.

There was some variability in the electrical resistivity in the metals studied, but thickness had been the main factor in the electrical resistance. As mentioned in Section 3.2, Hastelloy N was the thickest material measured to date at 1.041 mm, whereas the thinnest material measured by the NSEI group was at a thickness of 0.254 mm. Two extremes for the voltage drop was 1.27 mm section of Hastelloy N at the lowest measured temperature and a 2.54 mm section of Hastelloy X at the highest temperature measured. With these two cases, the voltage drop could be as small as 13 mV and up to 420 mV. Table 5.1 shows the absolute accuracy and resolution (bottom row) for the NI-USB-6251 for select voltages. Data in all studies were measured with the NI-USB-6251 set at ± 10 V range.

Table 5.1: Absolute accuracy and resolution of NI-USB-6251 for typical values of the voltage drops over 1.27 cm to 2.54 cm long sections.

ΔV	$u_{6251,AA}(\Delta V)$		$u_{6251,AA}(\Delta V)$		$u_{6251,AA}(\Delta V)$	
	FS: ± 0.5 V		FS: ± 1 V		FS: ± 10 V	
mV	V	%	V	%	V	%
10	1.7×10^{-5}	0.17	2.6×10^{-5}	0.26	2.67×10^{-4}	2.7
20	1.7×10^{-5}	0.085	2.7×10^{-5}	0.14	2.67×10^{-4}	1.3
50	1.8×10^{-5}	0.036	2.8×10^{-5}	0.06	2.68×10^{-4}	0.5
100	2.0×10^{-5}	0.020	2.9×10^{-5}	0.03	2.69×10^{-4}	0.269
200	2.3×10^{-5}	0.012	3.2×10^{-5}	0.02	2.71×10^{-4}	0.136
500	3.2×10^{-5}	0.0046	4.0×10^{-5}	0.01	2.77×10^{-4}	0.056
1000	—	—	5.3×10^{-5}	0.01	2.87×10^{-4}	0.029
$u_{6251,RES}$:	4.4×10^{-6}		8.8×10^{-6}		8.8×10^{-5}	

Unfortunately, $u_{6251,AA}$ was relatively large for signals under 500 mV where most values of the voltage drop will occur. This is due to the large offset error for the ± 10 V setting of

the DAQ. In Table 4.3, the coefficients for gain and offset errors for the NI-6251's absolute accuracy increase for lower full-scale settings of the NI-USB-6251. Yet, the magnitude of the full-scale setting affects the overall offset error. Setting the full-scale to a more appropriate range significantly reduces uncertainty from absolute accuracy. Resolution of the NI-USB-6251 does slightly add to the overall uncertainty of the NI-USB-6251 as the resolution uncertainty also decreases at the lower full-scale settings.

Table 5.2: Uncertainty components for DC current measurements in A.

I_{PSU}	V_{HES}	$u_{\text{HP6671A}}(I_{\text{PSU}})$	$u_{6251,AA}(V_{\text{HES}})$	$u_{I,\text{Total}}$
A	V	A	A	A
10	0.08	0.149	0.0335	1.8898
25	0.20	0.157	0.0339	1.8905
50	0.40	0.171	0.0344	1.8917
75	0.60	0.185	0.0349	1.8931
100	0.80	0.200	0.0345	1.8947
125	1.00	0.216	0.0359	1.8964
150	1.20	0.232	0.0364	1.8983
u_{HTA500S} :	1.860	A		
$u_{6251,\text{RES}}$:	0.0011	A		

The overall uncertainty in the HES sensor dominates the uncertainty in the current measurement process. Instead of examining Eq. 4.21 directly, Table 5.2 gives the uncertainty of the DC source (u_{HP6671A}), HES accuracy and linearity (u_{HTA500S}), and the NI-USB-6251 ($u_{6251,AA}$ and $u_{6251,\text{RES}}$). Again, full-scale setting of NI-USB-6251 was ± 10 V. For convenience, the uncertainties are converted to Amps, using the conversion factor

for Eq. 4.23. The total uncertainty in the rightmost column is similar Eq. 4.21, but without the repeatability error. The NI-USB-621 and DC source had a slight contribution to the uncertainty. HES uncertainty was determined at full scale input and the same for all values

Table 5.3: Standard uncertainty of TC measurements neglecting repeatability error. DAQ accuracy and resolution are constant for all temperatures.

T	$u_{K\text{-type}}(T)$		T	$u_{K\text{-type}}(T)$	
K	K	%	K	K	%
300	1.3	0.45	1000	3.1	0.43
500	1.3	0.44	1200	4.0	0.43
700	1.8	0.44	1300	4.4	0.43
900	2.7	0.43	1500	5.3	0.43

$u_{\text{USB-TC,ACC}}: 0.346 \text{ K}$

$u_{\text{USB-TC,RES}}: 6.9 \times 10^{-5} \text{ K}$

of the I_{PSU} . The HTA-500-S is rated up to 500 A DC. For typical DC current values for ohmic heating, less than half of the voltage output of the HES was used. When the NI-USB-6251 is set to a more suitable range this uncertainty to the measured current is negligible. Offset averaging will reduce the DC current uncertainty by half, but in the next section the uncertainty in the heat generated is still significant. The reduction in uncertainty in the HES can only be done by a using a better transducer such as a higher precision fluxgate magnetometer or shunt resistor.

Uncertainty in the temperature measurements increases from the uncertainty in the TC itself. Table 5.3 gives the uncertainty for errors in the TC and USB-TC DAQ card. The uncertainty in the K-type uncertainty was the only source that depends on the nominal

value of the temperature reading. Below 446.5 K, this uncertainty is constant as 1.3 K is larger than 0.43% of the temperature in degrees Celsius per Eq. 4.11. This uncertainty increased at elevated temperatures. DAQ uncertainties are constants. Offset averaging will decrease the uncertainty in the TC readings by a half. Spatial averaging decreases the temperatures by a factor of $1/N$, whereas non-uniformity of the temperatures at each location will add to this uncertainty.

5.3 Emissivity Calculation Uncertainty Budget

The number of specimen TCs and the multiple voltage taps (Figure 3.1) enable the calculation of emissivity in a variety of ways. Here we have considered two different sets of calculations on ‘as-received’ Alloy 718 Run #2. First case was applying Eq. 4.1 to area between TC #2 and TC #4. This section of the strip had dimensions of 1.27 cm by 2.54 cm by 0.409 mm. The voltage drop over the entire section was given by ΔV_{23} . Tables 5.4 and 5.5 gives the uncertainty budgets for the emissivity calculation for the lowest and highest temperatures measured, respectively. The DC currents required to heat Alloy 718 to its lowest and highest temperatures were 10 A and 65 A, respectively. Percent contribution is the ratio of the variance of each error source to the total variance. The combined uncertainty for the emissivity was rounded to two significant figures, whereas the uncertainties of input quantities and their sensitivity coefficients were unrounded for calculating combined uncertainty and percent contribution.¹⁵ The heat generated, hence heat radiated, is the dominate source of error with a contribution of 99.846%. The relative uncertainty in the heat generated was 13.46%. Relative uncertainty in the emissivity was around 13.26%. Uncertainty in the heat generated is too large to assess the contribution from other sources. Table 5.5, the uncertainty in heat generation is low enough to see the effects of other error

Table 5.4: Uncertainty budget for the emissivity calculation for Alloy 718 between TC #2 and TC #4 at the lowest temperature.

Qty	Average Value	Standard Uncertainty	Unit	D.O.F.	Sensitivity Coefficient		Percent Contribution
L_1	2.5400×10^{-2}	1.4575×10^{-5}	m	∞	-7.09437	m^{-1}	0.002
w_1	1.2700×10^{-2}	1.4575×10^{-5}	m	∞	-13.7461	m^{-1}	0.007
t_1	4.1×10^{-4}	1.4575×10^{-5}	m	∞	-13.7461	m^{-1}	0.007
T_1	563.63	0.62762	K	29	-1.408×10^{-3}	K^{-1}	0.131
T_2	310.03	0.94211	K	∞	2.3427×10^{-4}	K^{-1}	0.008
Q_1	0.624	0.08437	W	∞	0.28857	W^{-1}	99.845
ε	0.181	0.024		∞	—		100

Table 5.5: Uncertainty budget for the emissivity calculation for Alloy 718 between TC #2 and TC #4 at the highest temperature.

Qty	Average Value	Standard Uncertainty	Unit	D.O.F.	Sensitivity Coefficient		Percent Contribution
L_1	2.5400×10^{-2}	1.457×10^{-5}	m	∞	-10.788	m^{-1}	0.070
w_1	1.2700×10^{-2}	1.457×10^{-5}	m	∞	-20.9029	m^{-1}	0.264
t_1	4.1×10^{-4}	1.457×10^{-5}	m	∞	-20.9029	m^{-1}	0.264
T_1	1274.66	1.8609	K	256	-8.659×10^{-4}	K^{-1}	7.377
T_2	368.08	4.04448	K	1	2.0851×10^{-5}	K^{-1}	0.020
Q_1	27.12	0.56332	W	∞	1.0102×10^{-2}	W^{-1}	92.006
ε	0.2740	0.0059		∞	—		100

sources, particularly test section temperature. In Table 5.5, the relative uncertainties in the heat generated and emissivity were 2.06% and 2.15% respectively. The uncertainty in the emissivity at the highest temperature measured is below the uncertainty stated for the method in ASTM C835-06.

In Table 5.6, higher orders of the Taylor expansion offered no improvements to the standard uncertainty or expectation value. Table 5.6 gives the average value of emissivity and standard uncertainty from Eq. 2.9 and Eq. 2.10, respectively. A percent change of 0.004% and 0.005% in the standard uncertainty was seen for the lowest and highest emittance values of ‘as-received’ Alloy 718 Run #2 from the 1st to 2nd order Taylor’s Series. Rounding standard uncertainty to two significant figures gave the same values in Table 5.6. Higher orders derivatives for Eq. 4.1 with respect to Q_1 are zero, since Q_1 is linear. Higher order “sensitivity coefficients” will be small for the physical dimensions and temperatures as they are in the denominator of Eq. 4.1 and their power increases with each subsequent derivative.

Table 5.6: Emissivity and standard of Alloy 718 ‘as-received’ Run #2 from higher order Taylor Series.

Order	Average Value	Standard Uncertainty	Average Value	Standard Uncertainty
1	0.180197	0.0243899	0.274016	0.00593289
2	0.180202	0.0243909	0.274024	0.00593318
3	0.180202	0.0243909	0.274024	0.00593318

Results for the second case, based on calculating Eq. 4.1 over all TCs on the strip, are given in Tables 5.7 and 5.8. The voltage drop could not be measure directly and had to be obtained by summing the voltage drops between each adjacent TC pair ($\Delta V_1 + \Delta V_2 + \Delta V_3 + \Delta V_4$). The heat generated and the length scale according for all five TC pairs. The average specimen temperature is slightly higher, yet it has a lower uncertainty indicating better spatial uniformity to the new average value. Relative uncertainties for low and high

Table 5.7: Uncertainty budget for the emissivity calculation for Alloy 718 between TC #1 and TC #5 at the lowest temperature.

Qty	Average Value	Standard Uncertainty	Unit	D.O.F.	Sensitivity Coefficient	Percent Contribution
L_1	5.0800×10^{-2}	1.457×10^{-5}	m	∞	-3.5753 m ⁻¹	0.001
w_1	1.2700×10^{-2}	1.457×10^{-5}	m	∞	-13.855 m ⁻¹	0.007
t_1	4.1×10^{-4}	1.457×10^{-5}	m	∞	-13.855 m ⁻¹	0.007
T_1	563.51	0.56809	K	19	1.4193×10^{-3} K ⁻¹	0.108
T_2	310.03	0.94211	K	∞	2.3636×10^{-4} K ⁻¹	0.008
Q_1	1.26	0.16979	W	∞	0.144567 W ⁻¹	99.870
ϵ	0.182	0.025		∞	—	100

Table 5.8: Uncertainty budget for the emissivity calculation for Alloy 718 between TC #1 and TC #5 at the highest temperature.

Qty	Average Value	Standard Uncertainty	Unit	D.O.F.	Sensitivity Coefficient	Percent Contribution
L_1	5.0800×10^{-2}	1.457×10^{-5}	m	∞	-5.40659 m ⁻¹	0.018
w_1	1.2700×10^{-2}	1.457×10^{-5}	m	∞	-20.9516 m ⁻¹	0.270
t_1	4.1×10^{-4}	1.457×10^{-5}	m	∞	-20.9516 m ⁻¹	0.270
T_1	1275.73	1.56479	K	79	-8.672×10^{-4} K ⁻¹	5.325
T_2	368.08	4.04448	K	1	2.0828×10^{-5} K ⁻¹	0.021
Q_1	54.6	1.13317	W	∞	5.0338×10^{-3} W ⁻¹	94.097
ϵ	0.2747	0.0059		∞	—	100

emittance were 13.74% and 2.08%, respectively. These values are similar to the calculation between TC #2 and TC #4. A closer look at the uncertainty budgets for the heat generated for the highest emissivity measurement for Alloy 718 are provided in Tables 5.9, 5.10, and

5.11, respectively. In Tables 5.9 and 5.10, the uncertainty in voltage drop between TC #2 and TC #4 is higher by adding the voltage drop between TC #2 and TC# 3 and TC#3 and TC #4 compared to measuring it directly. However, the uncertainty in the heat generated is similar due to the dominance of the uncertainty in the DC current. The percent contribution of the voltage drops increases accordingly as shown in Tables 5.9 and 5.10. When adding the voltage drops for all sections, the variance contribution of all the voltage drops approaches value of the voltage in Table 5.9.

In both cases, the degrees of freedom decrease the wall temperatures and increase with the specimen temperature from low to high emittance values. In Eq. 4.25, the total uncertainty in the TC measurements and spread in the spatial averaging are the only contributing factors. Uncertainties in the measurements have high degrees of freedom as many error sources are Type B. Spatial averaging has degrees of freedom of one less than the number to TCs. The dominance of either term shifts the degrees of freedom towards that error source. Wall temperatures become less uniform at the higher temperatures, but the whole specimen temperatures become slightly more uniform.

Table 5.9: Uncertainty budget for the heat generated between TC #2 to TC #4 using the voltage drop measured between TC #2 and TC #4.

Qty	Average Value	Standard Uncertainty	Unit	D.O.F.	Sensitivity Coefficient	Percent Contribution
ΔV_{23}	4.1960×10^{-1}	6.92445×10^{-4}	V	227	64.6443 W V ⁻¹	0.631
I	64.64	1.3383	A	∞	4.1960×10^{-1} W A ⁻¹	99.369
Q_1	27.12	0.56	W	∞	—	100

Table 5.10: Uncertainty budget for the heat generated between TC #2 to TC #4 by adding the voltage drops between TC #2 to TC #3 and TC #3 to TC #4.

Qty	Average Value	Standard Uncertainty	Unit	D.O.F.	Sensitivity Coefficient		Percent Contribution
ΔV_2	2.1010×10^{-1}	6.54746×10^{-4}	V	236	64.6443	$W V^{-1}$	0.554
ΔV_3	2.1196×10^{-1}	7.43838×10^{-4}	V	213	64.6443	$W V^{-1}$	0.716
I	64.64	1.3383	A	∞	4.2206×10^{-1}	$W A^{-1}$	98.730
Q_1	27.28	0.57	W	∞	—		100

Table 5.11: Uncertainty budget for the heat generated between TC #1 to TC #5 by adding the voltage drops measured between adjacent TC pair.

Qty	Average Value	Standard Uncertainty	Unit	D.O.F.	Sensitivity Coefficient		Percent Contribution
ΔV_1	2.1188×10^{-1}	6.5542×10^{-4}	V	236	64.6443	$W V^{-1}$	0.140
ΔV_2	2.1010×10^{-1}	6.5475×10^{-4}	V	236	64.6443	$W V^{-1}$	0.140
ΔV_3	2.1196×10^{-1}	7.4384×10^{-4}	V	213	64.6443	$W V^{-1}$	0.180
ΔV_4	2.1008×10^{-1}	7.4024×10^{-4}	V	214	64.6443	$W V^{-1}$	0.178
I	64.64	1.3383	A	∞	5.5442×10^{-1}	$W A^{-1}$	99.362
Q_1	54.6	1.1	W	∞	—		100

5.4 Uncertainty in Data Sets

The uncertainty in total hemispherical data decreases at higher temperatures where the higher currents can be more precisely measured. This can be seen with data obtained on Hastelloy X at a thickness of 0.254 mm thick compared to data on Alloy 718 with a thickness of 0.409 mm. Figure 5.1 shows plots of ‘as-received’ Hastelloy X (top) and ‘as-received’ Alloy 718 (bottom). The light blue data points have a relative uncertainty in

excess of 5% as stipulated in ASTM C835-06. Hastelloy X required up to 34 A to reach maximum temperature of 1035 K, while Alloy 718 needed 65 A to achieve a temperature of 1275 K. Eight out of thirteen points in Hastelloy X have a relative uncertainty more than 5%. The lowest temperature at point for Hastelloy X has an uncertainty of 31%. Only the first two points in Alloy 718 have failed to comply to the stated uncertainty of 5%. However, the uncertainty in the heat generated is higher than 1% in all the data per ASTM C835-06. Since the faces along the thickness, or edges, are not in the same surface condition as the rest of the strip, a thick strip can cause a large error in the measured emissivity as Eq. 4.1 assumes a uniform surface.³⁶ Here a thin strip is desired to minimize this error.

The above trends are consistent with the surfaces treatments on the alloys by the NSEI group. A material with a high total hemispherical emissivity will also require more current to heat to a desired temperature. In the data so far, this effect is not as pronounced as the electrical resistance of the specimens. Figure 5.2 compares ‘as-received’ Alloy 718 to a sample of Alloy 718 that was sandblasted with 220-grit alumina beads and coated with NBG-18 graphite powder. The latter sample exhibited the highest emissivity out of all the other treatments including oxidation in air at 1073 K.²⁶ For the lowest temperatures in the high emittance case of Alloy 718 the uncertainty is still greater than 5%. While Alloy 718 sample requires more current to heat, the lower temperature points were still obtained with currents less than 18 A where the relative uncertainty in DC current is large. The graphite coated and sandblasted achieves an acceptable precision at 750 K, unlike the ‘as-received’ Alloy 718.

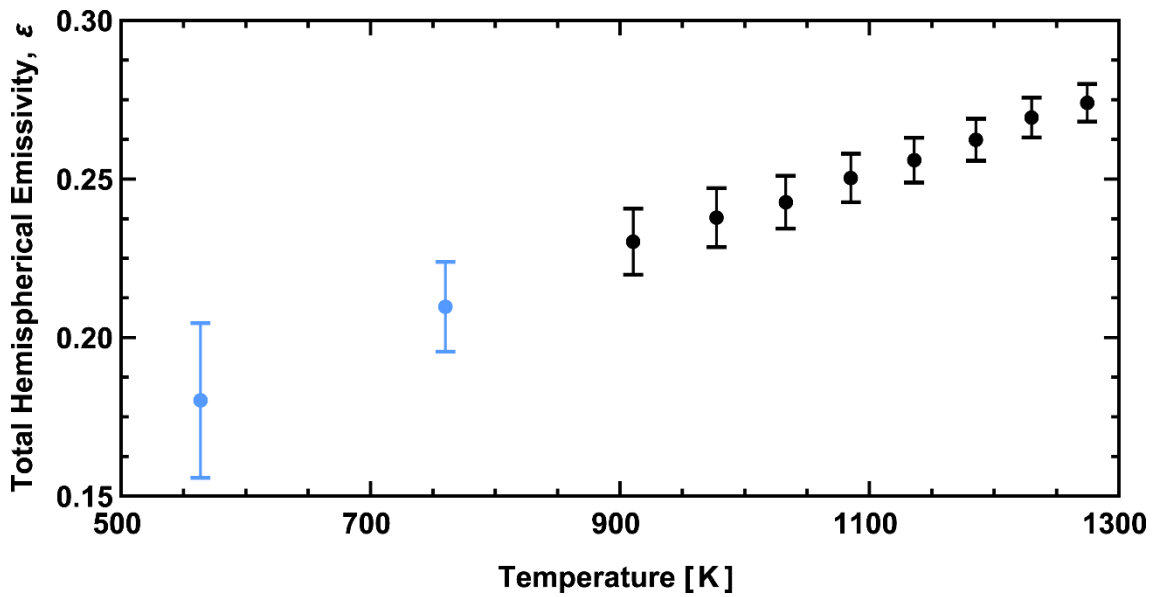
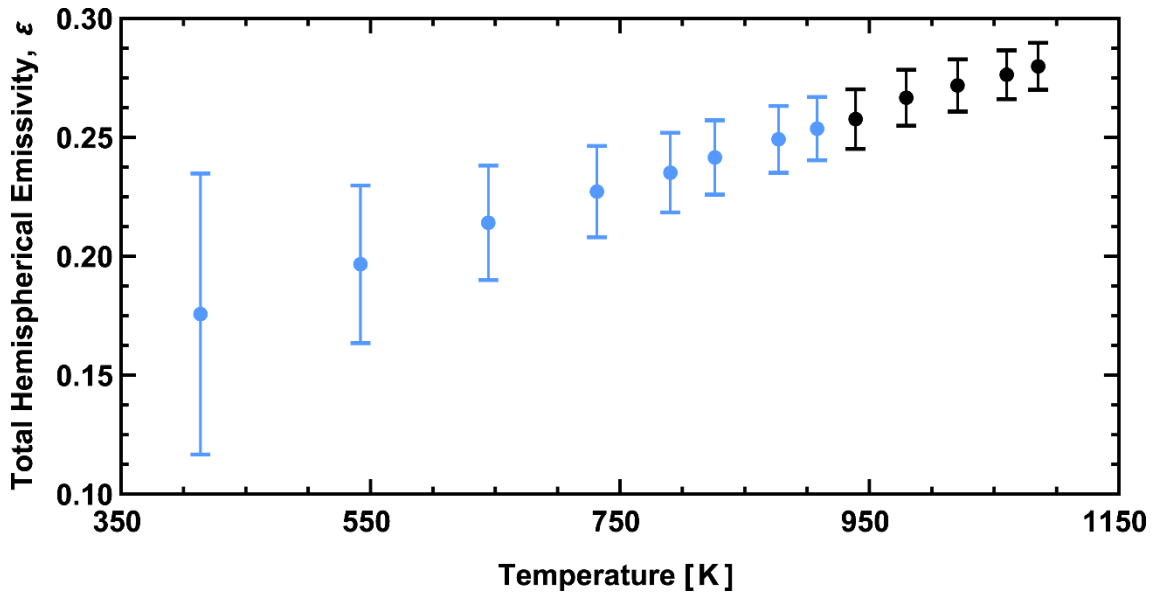


Figure 5.1: Standard uncertainties in the form of errors bars for 0.254 mm thick Hastelloy X (top graph) and 0.409 mm thick Inconel 718 (bottom graph). Blue points are data with emissivity with relative uncertainty greater than 5%. Both surfaces are ‘as-received’.

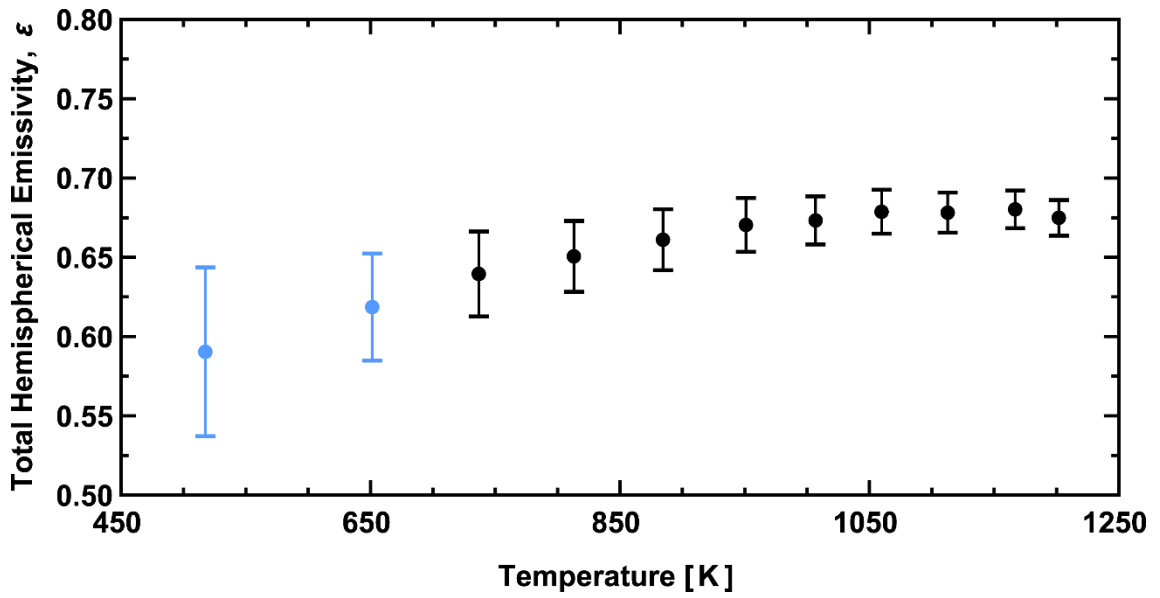
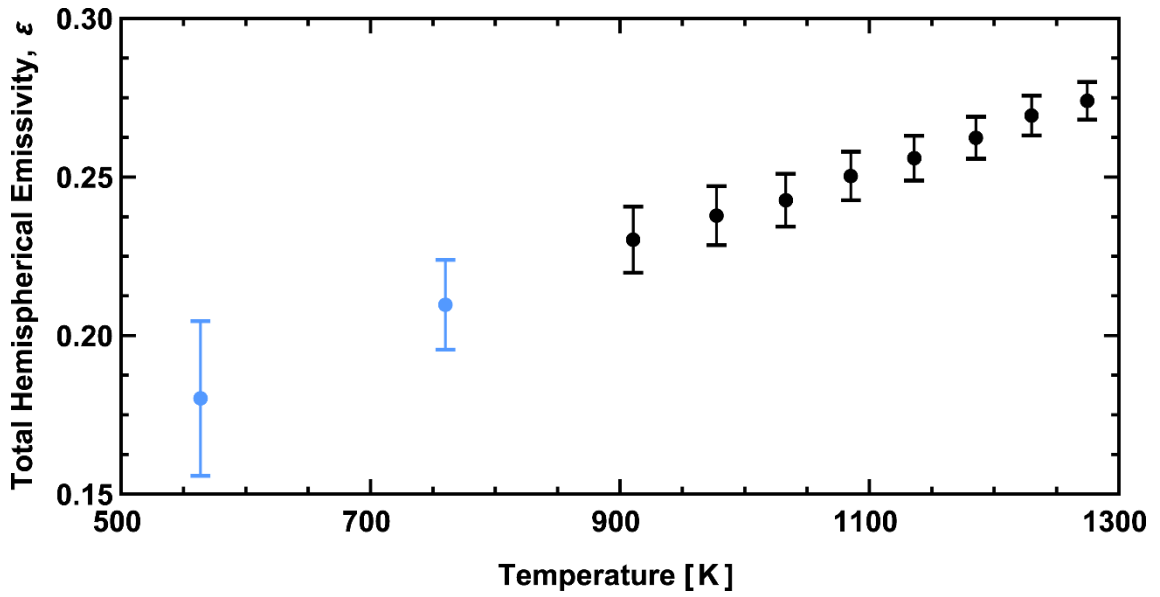


Figure 5.2: Standard uncertainties in the form of errors bars for Alloy 718 for a low-emittance (top graph) and high-emittance surface conditions (bottom graph). Blue points are data with emissivity with a relative uncertainty greater than 5%.

Finally, the analysis was applied to data on oxidized SS 316L. Samples were oxidized at a temperature of 973 K with calorimeter itself by venting room air in the chamber.²⁵ With the error bars, it is easier to deduce the change in emissivity to surface condition. Between 650 K and 850 K, the total hemispherical emissivity for 10 minutes and 15 minutes oxidized samples are quite similar and are within the experimental uncertainty of the measurements. Above 900 K, the emissivity for 15 min. oxidized has a lower emissivity than SS 316L oxidized for 10 min. The error bars allow one to infer the other causes in the difference of the materials emissivity. This can direct help direct further investigation into the material or surface effects on emissivity.

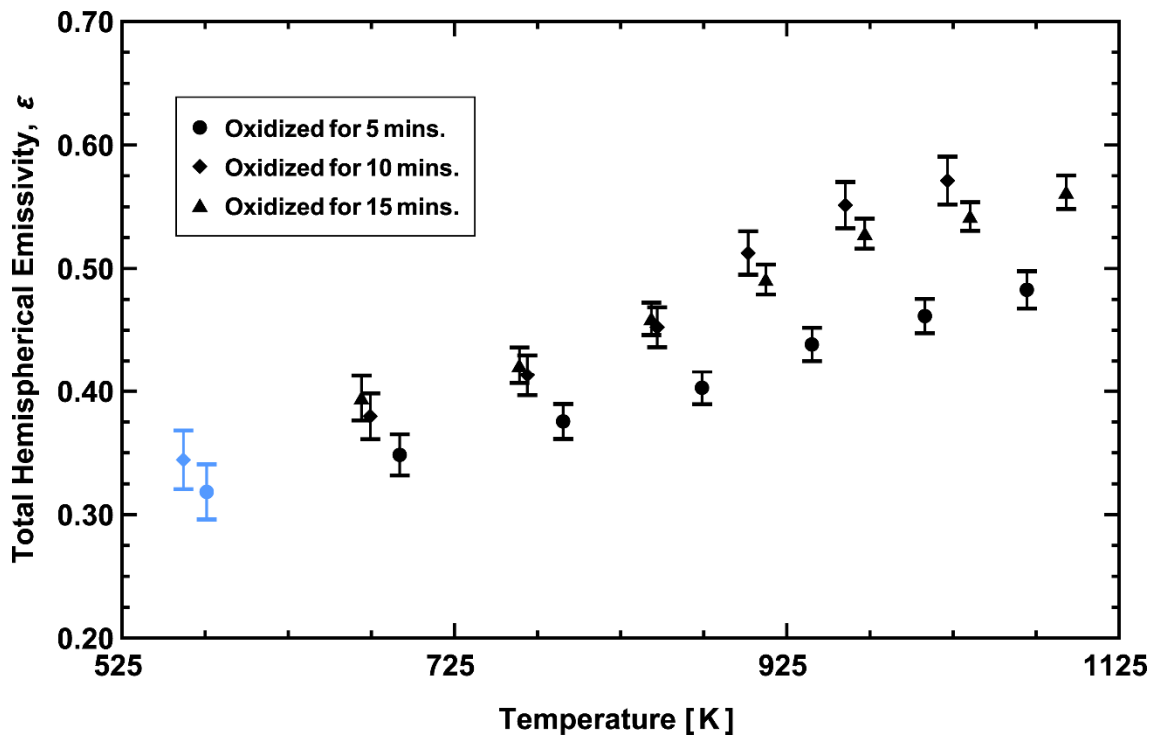


Figure 5.3: Standard uncertainties in emissivity for oxidized SS 316S in the form of errors bars.

CHAPTER 6

CONCLUSIONS

Analysis of data from the NSEI group has shown that uncertainty in the electric current is a dominate source of uncertainty for the heat generated and thus emissivity. It is preferable to measure the entire voltage drop directly, but adding voltage drops of adjacent sections is acceptable as the uncertainty in voltage measurements is low and a small contributor to the uncertainty in the heat generated. As Alloy 718 is thinner compared to the SS 316L, the uncertainties in the emissivity of SS 316L will have similar trends in the overall uncertainty as the samples need more DC current to obtain similar temperatures.

Though the uncertainty in the TCs appear to have a small effect, calibrations are needed to fully address their accuracy in the measurement of total hemispherical emissivity. Ideally, this includes calibrating the desired TC type spot-welded to the material to be measured. A specialized study maybe sufficient if specific TC types do not depend on the metal they are welded and drift during the measurement.

The challenges in presenting data for uncertainty analysis for this type of measurement requires a different approach than explored in this dissertation. The ASTM C835-06 has requirements for reporting total hemispherical data. This includes the dimensions of the test section, the voltage drops and current through the test section, and average specimen and wall temperatures. To be consistent with the GUM, error sources should be listed and their justifications given if there is no supporting documentation. Uncertainty budgets for the heat generated along with any systematic effects need to be given for at least the lowest and highest temperature show the minimum and maximum values for the uncertainty. For shunt resistors or hall effect sensors, details on their setup

and description of their temperature monitoring or control need to be given for determining temperature effects in uncertainty in measured currents. Uncertainty for emissivity and the input quantities can then be tabulated per ASTM C835-06. The sensitivity coefficients for the standard uncertainty in the emissivity can be derived separately and evaluated using tabulated results. As the W-S formula was not rigorously justified for each step, coverage factors need to be used to report expanded uncertainties from this analysis.

The analysis used in this dissertation can be further refined. Interlaboratory testing of other ASTM C835-06 designs may identify and quantify sources error not possible from analyzing the system in this study. Intralaboratory testing with the two calorimeters by the NSEI group may be too similar to determine such errors. Changing the TC type and ohmic heating to AC currents could be sufficient to determining other sources of uncertainty or one system to AC current heating should be useful in assessing the offset correction used for the specimen TCs for DC current heating. Additionally, expressions for the systematic effects can be refined and their uncertainty determined to see how they will add to the uncertainties determined in this study.

APPENDIX

MATERIAL DATA

A.1 Thermal Conductivity

Thermal conductivity data given here was used in for calculating heat losses from thermal conductivity from with the specimen and from the TC wires. Data for alumel and chormel (chromel-P) from 100 K to 450 K was reported by Sundqvist⁵⁰. Above 450 K, data for alumel and chormel (chromel-P) was taken from Touloukan et al.⁵¹ Hastelloy X thermal conductivity over the temperature range of 673.15 K to 1273.15 K was obtained for the manufacture's brochure. Tables A.1, A.2, and A.3 provide the thermal conductivity of Hastelloy X, alumel, and chromel (chromel-P), respectively. Note all quantities are given in SI units.

Table A.1: Thermal conductivity of Hastelloy X.

T	λ
K	$\text{W m}^{-1} \text{K}^{-1}$
673.15	16.9
873.15	20.9
973.15	22.8
1073.15	24.8
1173.15	26.7
1273.15	28.7

Table A.2: Thermal conductivity of alumel.

T K	λ $\text{W m}^{-1} \text{K}^{-1}$	T K	λ $\text{W m}^{-1} \text{K}^{-1}$
100.00	19.4	350.00	30.6
125.00	21.0	375.00	31.1
150.00	22.5	400.00	31.6
175.00	24.2	422.00	31.8
200.00	25.7	425.00	31.9
225.00	26.8	450.00	32.6
250.00	27.7	473.20	31.80
275.00	28.5	573.20	35.90
300.00	29.2	673.20	38.10
325.00	29.9	773.20	41.20

Table A.3: Thermal conductivity of chormel.

T K	λ $\text{W m}^{-1} \text{K}^{-1}$	T K	λ $\text{W m}^{-1} \text{K}^{-1}$
100.00	12.9	350.00	18.4
125.00	13.2	375.00	19.0
150.00	13.7	400.00	19.7
175.00	14.3	425.00	20.3
200.00	14.9	450.00	21.0
225.00	15.5	473.20	20.9
250.00	16.1	573.20	22.8
275.00	16.7	673.20	24.7
300.00	17.3	773.20	26.6

A.2 Emissivity

Emissivity data given here was used in for calculating the heat loss TC wires. Saskia et al.⁵² reported emissivity for alumel and chormel (chromel-P) for the temperature range 360 K to 760 K. Tables A.4 and A.5 provide the total hemispherical emissivity of alumel and chromel (chromel-P), respectively. Note all quantities are given in SI units.

Table A.4: Total hemispherical emissivity of alumel.

<i>T</i> K	ϵ —	<i>T</i> K	ϵ —
360.00	0.077	580.00	0.112
380.00	0.080	600.00	0.115
400.00	0.083	620.00	0.118
420.00	0.087	640.00	0.121
440.00	0.090	660.00	0.124
460.00	0.094	680.00	0.127
480.00	0.097	700.00	0.130
500.00	0.100	720.00	0.133
520.00	0.103	740.00	0.136
540.00	0.106	760.00	0.139
560.00	0.109	—	—

Table A.5: Total hemispherical emissivity of chormel.

T	ϵ	T	ϵ
K	—	K	—
360	0.096	580	0.126
380	0.100	600	0.128
400	0.103	620	0.130
420	0.106	640	0.132
440	0.109	660	0.134
460	0.112	680	0.136
480	0.115	700	0.138
500	0.117	720	0.140
520	0.120	740	0.142
540	0.122	760	0.144
560	0.124	—	—

BIBLIOGRAPHY

1. M. A. Davies, T. Ueda, R. M'Saoubi, B. Mullany, and A. L. Cooke. "On The Measurement of Temperature in Material Removal Processes." *CIRP Annals*, vol. 56, no. 2, 2007, pp. 581-604, <<https://doi.org/10.1016/j.cirp.2007.10.009>>
2. P. R. Muniz, R. d. A. Kalid, S. P. Cani, and R. d. S. Magalhães. "Handy method to estimate uncertainty of temperature measurement by infrared thermography." vol. 53, SPIE, 2014, p. 7. <<https://doi.org/10.1117/1.OE.53.7.074101>>.
3. T. K. West, and S. Hosder. "Uncertainty Quantification of Hypersonic Reentry Flows with Sparse Sampling and Stochastic Expansions." *Journal of Spacecraft and Rockets*, vol. 52, no. 1, 2014, pp. 120-133, <<https://doi.org/10.2514/1.A32947>>
4. R. L. Iman, and J. C. Helton. "An Investigation of Uncertainty and Sensitivity Analysis Techniques for Computer Models." *Risk Anal.*, vol. 8, no. 1, 1988, pp. 71-90, <<https://doi.org/10.1111/j.1539-6924.1988.tb01155.x>>
5. M. M. R. Williams. "A probabilistic study of the influence of parameter uncertainty on thermal radiation heat transfer." *Int. J. Heat Mass Transf.*, vol. 53, no. 7, 2010, pp. 1461-1472, <<https://doi.org/10.1016/j.ijheatmasstransfer.2009.12.00>>
6. ASTM International, *Standard Test Method for Total Hemispherical Emittance of Surfaces up to 1400°C*. C835-06(2013), ASTM International, West Conshohocken, PA. 2013. Web. <<https://doi.org/10.1520/C0835>>, 28 Nov. 2017.
7. E. C. Compton. NASA-TM-87681, "Evaluation of a standard test method for total hemispherical emittance of surfaces from 293K to 1673K." Technical report, National Aeronautics and Space Administration, 1986. NASA Technical Reports Server, <<https://ntrs.nasa.gov/archive/nasa/casi.ntrs.nasa.gov/19860012189.pdf>>, 22 Nov. 2017.
8. T. Fu, P. Tan, and C. Pang. "A steady-state measurement system for total hemispherical emissivity." *Meas. Sci. Technol.*, vol. 23, no. 2, 2012, p. 025006, <<https://doi.org/10.1088/0957-0233/23/2/025006>>
9. L. d. Campo, R. B. Pérez-Sáez, L. González-Fernández, and M. J. Tello. "Combined standard uncertainty in direct emissivity measurements." *J. Appl. Phys.*, vol. 107, no. 11, 2010, p. 113510, <<https://doi.org/10.1063/1.3431541>>

10. P. Honnerová, J. Martan, and M. Honner. "Uncertainty determination in high-temperature spectral emissivity measurement method of coatings." *Appl. Therm. Eng.*, vol. 124, no. Supplement C, 2017, pp. 261-270, <<https://doi.org/10.1016/j.applthermaleng.2017.06.022>>
11. J. R. Howell, R. Siegel, and M. P. Mengüç. *Thermal Radiation Heat Transfer*. 5th edition, CRC Press, 2011.
12. Y. S. Touloukian, and D. P. DeWitt. *Thermal Radiative Properties : Metallic Elements and Alloys*. vol. 7, University Microfilms International, 1990. Defense Technical Information Center, <<http://www.dtic.mil/get-tr-doc/pdf?AD=ADA951941>>, 28 Nov. 2017.
13. G. Kirchhoff. "I. On the relation between the radiating and absorbing powers of different bodies for light and heat." *The Lond., Edinb., and Dublin Philos. Mag. and J. of Sci.*, vol. 20, no. 130, 1860, pp. 1-21, <<https://doi.org/10.1080/14786446008642901>>
14. H. P. Baltes. "I On the Validity of Kirchhoff'S Law of Heat Radiation for a Body in a Nonequilibrium Environment." *Prog. Opt.*, edited by E. Wolf, vol. 13, Elsevier, 1976, pp. 1-25.
15. BIPM, IEC, IFCC, ILAC, ISO, IUPAC, IUPAP, and OIML. JCGM 100: 2008, "Evaluation of measurement data—guide for the expression of uncertainty in measurement (GUM 1995 with Minor Corrections)." Technical report, JCGM, 2008, <https://www.bipm.org/utils/common/documents/jcgm/JCGM_100_2008_E.pdf>, 22 Nov. 2017
16. R. S. Figliola, and D. E. Beasley. *Theory and design for mechanical measurements*. Wiley, 2011.
17. S. V. Gupta. *Measurement uncertainties : physical parameters and calibration of instruments*. Springer, 2012.
18. J. Zhang. "The calculating formulae, and experimental methods in error propagation analysis." *IEEE Trans. Reliab.*, vol. 55, no. 2, 2006, pp. 169-181, <<https://doi.org/10.1109/TR.2006.874920>>
19. R. H. Dieck. "Measurement uncertainty models." *ISA Trans.*, vol. 36, no. 1, 1997, pp. 29-35, <[https://doi.org/10.1016/S0019-0578\(97\)00004-9](https://doi.org/10.1016/S0019-0578(97)00004-9)>

20. R. B. Abernethy, and B. Ringhiser. "The history and statistical development of the new ASME-SAE-AIAA-ISO measurement uncertainty methodology." *Proc. AIAA/SAE/ASME/ASME 21st Joint Propulsion Conf*, 1985, pp. 8-10. <<http://citeseerx.ist.psu.edu/viewdoc/download?doi=10.1.1.197.9544&rep=rep1&type=pdf>>, 28 Nov. 2017.

21. A. Possolo. "Simple Guide for Evaluating and Expressing the Uncertainty of NIST Measurement Results." *NIST Technical Note*, 1900, <<https://dx.doi.org/10.6028/NIST.TN.1900>>

22. R. Dieck, W. Steele, and G. Osolsobe, *Test Uncertainty*. ASME PTC 19.1-2005, American Society of Mechanical Engineers, New York, NY. 2005. Print.

23. National Aeronautics and Space Administration, *Measurement Uncertainty Analysis Principles and Methods, NASA Measurement Quality Assurance Handbook - ANNEX 3*. NASA-HDBK-8739.19-3, 2010-07-13, 2010. Web. <<https://standards.nasa.gov/standard/nasa/nasa-hdbk-873919-4>>, 28 Nov. 2017.

24. H. Castrup. "A Welch-Satterthwaite relation for correlated errors." *Measurement Science Conference*, 26 Mar. 2010. 2010. <<https://pdfs.semanticscholar.org/7c9a/41aa3cce0bb79e69bc820369c4e2ec1a7e3c.pdf>>, 28 Nov. 2017.

25. T. S. Hunnewell, K. L. Walton, S. Sharma, T. K. Ghosh, R. V. Tompson, D. S. Viswanath, and S. K. Loyalka. "Total Hemispherical Emissivity of SS 316L with Simulated Very High Temperature Reactor Surface Conditions." *Nucl. Technol.*, vol. 198, no. 3, 2017, pp. 293-305, <<https://doi.org/10.1080/00295450.2017.1311120>>

26. B. P. Keller, S. E. Nelson, K. L. Walton, T. K. Ghosh, R. V. Tompson, and S. K. Loyalka. "Total hemispherical emissivity of Inconel 718." *Nucl. Eng. Des.*, vol. 287, 2015, pp. 11-18, <<https://doi.org/10.1016/j.nucengdes.2015.02.018>>

27. R. K. Maynard, N. M. Mokgalapa, T. K. Ghosh, R. V. Tompson, D. S. Viswanath, and S. K. Loyalka. "Hemispherical Total Emissivity of Potential Structural Materials for Very High Temperature Reactor Systems: Haynes 230." *Nucl. Technol.*, vol. 179, no. 3, 2012, pp. 429-438, <<https://doi.org/10.13182/NT11-5>>

28. A. J. Gordon, K. L. Walton, T. K. Ghosh, S. K. Loyalka, D. S. Viswanath, and R. V. Tompson. "Hemispherical total emissivity of Hastelloy N with different surface conditions." *J. Nucl. Mater.*, vol. 426, no. 1-3, 2012, pp. 85-95, Scopus, <<https://doi.org/10.1016/j.jnucmat.2012.03.026>>

29. R. K. Maynard, T. K. Ghosh, R. V. Tompson, D. S. Viswanath, and S. K. Loyalka. "Total Hemispherical Emissivity of Potential Structural Materials for Very High Temperature Reactor Systems: Hastelloy X." *Nucl. Technol.*, vol. 172, no. 1, 2010, pp. 88-100, <<https://doi.org/10.13182/NT10-6>>

30. W. H. Askwyth, R. J. Hayes, R. D. House, and G. Mikk. PWA-2206(VOL.1), "Determination of the emissivity of materials." Technical report, Pratt and Whitney Aircraft, 1962. SciTech Connect, <<https://doi.org/10.2172/4051368>>, 28 Nov. 2017

31. G. D. Gordon, and A. London. "Emittance Measurements at Satellite Temperatures." *Symposium on Measurement of Thermal Radiation Properties of Solids*, edited by J. C. Richmond, vol. NASA-SP-31, 5-7 Sep. 1962 1963, pp. 147-150.

32. S. X. Cheng, X. S. Ge, C. C. Yao, J. W. Gao, and Y. Z. Zhang. "Research on the validity of the steady-state calorimeter for measuring the total hemispherical emissivity of solids." *Meas. Sci. Technol.*, vol. 4, no. 7, 1993, p. 721, <<http://stacks.iop.org/0957-0233/4/i=7/a=002>>

33. S. Dushman. *Scientific Foundations of Vacuum Technique*. edited by James Martin Lafferty, 2nd edition, John Wiley & Sons, 1962.

34. J. F. O'Hanlon. *A User's Guide to Vacuum Technology*. 3rd edition, John Wiley & Sons, 2003.

35. A. Roth. *Vacuum technology*. 2nd rev. ed. edition, North-Holland Pub. Co., 1990.

36. K. E. Nelson, and J. T. Bevans. "Errors of the Calorimetric Method of Total Emittance Measurement." *Symposium on Measurement of Thermal Radiation Properties of Solids*, edited by J. C. Richmond, vol. NASA-SP-31, 5-7 Sep. 1962 1963, pp. 55-65.

37. G. L. Abbott. "Total Normal and Total Hemispherical Emittance of Polished Metals." *Symposium on Measurement of Thermal Radiation Properties of Solids*, edited by J. C. Richmond, vol. NASA-SP-31, 5-7 Sep. 1962 1963, pp. 293-306.

38. J. T. Bevans, and K. E. Nelson. "Nongray Error in Total Emittance Measurements." *AIAA J.*, vol. 1, no. 8, 1963, pp. 1966-1967, <<https://doi.org/10.2514/3.1982>>

39. L. del Campo, R. B. Pérez-Sáez, L. González-Fernández, X. Esquisabel, I. Fernández, P. González-Martín, and M. J. Tello. "Emissivity measurements on aeronautical

- alloys." *J. Alloy Compd.*, vol. 489, no. 2, 2010, pp. 482-487, <<https://doi.org/10.1016/j.jallcom.2009.09.091>>
40. ASTM International, *Standard Specification and Temperature-Electromotive Force (emf) Tables for Standardized Thermocouples*. E230/E230M-12, ASTM International, West Conshohocken, Pa. 2012. Web. <https://doi.org/10.1520/E0230_E0230M-12>, 28 Nov. 2017.
 41. German Institute for Standardization, Geometrical product specifications (GPS) – Callipers –Maximum permissible errors,English translation of DIN 862:2015-03. DIN 862:2015-03, Berlin, Germany. 2015. Print.
 42. D. Saecker, and R. Klinke. "Simultaneous Improvement of Accuracy and Efficiency." *2012 NCSL International Workshop & Symposium*, 29 Jul. - 2 Aug. 2012. *The Business End of Metrology Quality and Testing*.
 43. National Instruments. "NI 6251 Device Specifications." 2016, p. 26. <<http://www.ni.com/pdf/manuals/375213c.pdf>>, 22 Nov. 2017.
 44. G. A. Greene, C. C. Finfrock, and T. F. Irvine. "Total hemispherical emissivity of oxidized Inconel 718 in the temperature range 300–1000°C." *Exp. Therm. Fluid Sci.*, vol. 22, no. 3, 2000, pp. 145-153, <[https://doi.org/10.1016/S0894-1777\(00\)00021-2](https://doi.org/10.1016/S0894-1777(00)00021-2)>
 45. R. Park, R. Carroll, P. Bliss, G. Burns, R. Desmaris, F. Hall, M. Herzkovitz, D. MacKenzie, E. McGuire, R. Reed, L. Sparks, and T. Wang, editors. *Manual on the Use of Thermocouples in Temperature Measurement*. 4th edition, ASTM International, 1993. Sponsored by ASTM Committee E20 on Temperature Measurement, <<https://doi.org/10.1520/MNL12-4TH-EB>>
 46. ASTM International, *Standard Guide for Thermocouple Verification*. E2846-14, West Conshohocken, PA. 2014. Web. <<https://doi.org/10.1520/E2846-14>>, 28 Nov 2017.
 47. R. E. Bentley. *Theory and Practice of Thermoelectric Thermometry*. vol. 3, Springer, 1998. *Handbook of Temperature Measurement*.
 48. Measurement Computing Corporation. "USB-TC: Specifications." Rev 10A edition, 2016. <<https://www.mccdaq.com/pdfs/manuals/USB-TC.pdf>>, 22 Nov. 2017.
 49. Keysight Technical Support. e-mail message to technical support, June 28, 2017.

50. B. Sundqvist. "Thermal diffusivity and thermal conductivity of Chromel, Alumel, and Constantan in the range 100–450 K." *J. Appl. Phys.*, vol. 72, no. 2, 1992, pp. 539-545, <<https://doi.org/10.1063/1.351885>>
51. Y. S. P. Touloukian, R. W., C. Y. Ho, and P. G. Klemens. *Thermal Conductivity: Metallic Elements and Alloys*. vol. 1, University Microfilms International, 1970. Defense Technical Information Center, < <http://www.dtic.mil/get-tr-doc/pdf?AD=ADA951935>>, 28 Nov. 2017.
52. S. Sasaki, H. Masuda, M. Higano, and N. Hishinuma. "Simultaneous measurements of specific heat and total hemispherical emissivity of chromel and alumel by a transient calorimetric technique." *International Journal of Thermophysics*, vol. 15, no. 3, 1994, pp. 547-565, <<https://doi.org/10.1007/BF01563713>>

VITA

Kyle L. Walton was born to John and Susan Walton in West Plains, Missouri, United States of America, on December 15, 1983. He graduated from Alton R-IV High School in Alton, Missouri in 2002. He attended the University of Missouri where he obtained a bachelors of science degree in physics and mathematics with departmental honors in both majors on December 2006. His student job at the University of Missouri Research Reactor (MURR) and undergraduate research led him to pursue a career in nuclear engineering. Kyle continued his post-baccalaureate education at the University of Missouri in nuclear engineering under the Nuclear Science and Engineering Institute. He earned his master of science in nuclear engineering with an emphasis health physics in December 2009. He completed his Ph.D. in nuclear engineering in December of 2017.